

# Growth of Large-Area Graphene Single Crystals in Confined Reaction Space with Diffusion-Driven Chemical Vapor Deposition

Chiao-Chen Chen,<sup>\*,†,‡</sup> Chia-Jung Kuo,<sup>†</sup> Chun-Da Liao,<sup>†</sup> Chin-Fu Chang,<sup>†</sup> Chi-Ang Tseng,<sup>†</sup> Chia-Rung Liu,<sup>†</sup> and Yit-Tsong Chen<sup>\*,†,§</sup>

<sup>†</sup>Department of Chemistry, National Taiwan University, No. 1, Sec. 4, Roosevelt Road, Taipei 106, Taiwan

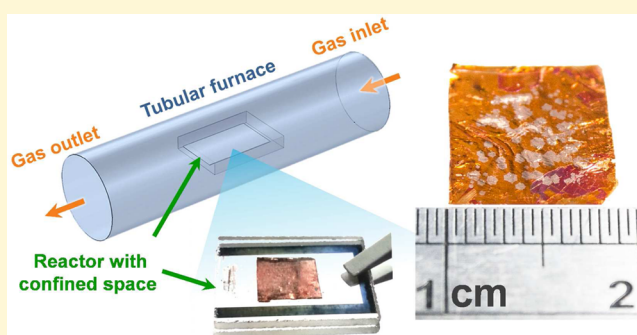
<sup>‡</sup>Department of Chemistry, Tamkang University, No. 151, Yingzhuang Road, New Taipei City 25137, Taiwan

<sup>§</sup>Institute of Atomic and Molecular Sciences, Academia Sinica, P.O. Box 23-166, Taipei 106, Taiwan

## Supporting Information

**ABSTRACT:** To synthesize large-area graphene single crystals, we specifically designed a low-pressure chemical vapor deposition (LPCVD) reactor with confined reaction space (L 22 mm × W 13 mm × H 50 μm). Within the confined reaction space, a uniform distribution of reactant concentrations, reduced substrate roughness, and the shift of growth kinetics toward a diffusion-limited regime can be achieved, favoring the preparation of large-area, high-quality graphene single crystals. The gas flow field and mass transport pattern of reactants in the LPCVD system simulated with a finite element method support the advantages of using this confined reaction room for graphene growth. Using this space-

confined reactor together with the optimized synthesis parameters, we obtained monolayer, highly uniform, and defect-free graphene single crystals of up to ~0.8 mm in diameter with the field-effect mobility of  $\mu_{\text{EF}} \sim 4800 \text{ cm}^2 \text{ V}^{-1} \text{ s}^{-1}$  at room temperature. In addition, structural design of the confined reaction space by adjusting the reactor's dimensions is of facile controllability and scalability, which demonstrates the superiority and preference of this method for industrial applications.



## INTRODUCTION

The metal catalytic growth of graphene via chemical vapor deposition (CVD) reaction is considered as one of the most promising methods to enable mass production of high-quality graphene films.<sup>1–5</sup> However, most of these CVD processes produce polycrystalline graphene composed of relatively small graphene grains.<sup>6</sup> The presence of structural variations in graphene, such as grain boundaries and multilayer regions, will cause degradations in both the physical and the chemical properties of a synthesized graphene, including restricted electrical mobility,<sup>7</sup> suppressed thermal conductivity,<sup>8</sup> reduced sheet strength,<sup>9,10</sup> and less oxidation resistance.<sup>11</sup> Considerable efforts have been made recently to prepare large single-crystal graphene that is free of structural variations induced by the coalescence of different graphene grains. The key point to obtain large single-crystal graphene is to reduce the nucleation density in the graphene growth; to this end, several strategies have been implemented in the CVD methods. For instance, a trace amount of oxygen introduced onto a catalytic Cu substrate right before the graphene growing reaction was demonstrated to be able to reduce the nucleation density significantly and to promote the graphene growth rate.<sup>12</sup> In addition, suppressing the Cu sublimation in low-pressure CVD (LPCVD) system,<sup>13,14</sup> melting followed by resolidifying Cu substrates,<sup>15</sup> and annealing Cu substrates under high pressure

of pure H<sub>2</sub> for a prolonged time<sup>16</sup> could reduce the surface roughness of Cu foils effectively, resulting in low nucleation density. Other methods, by using Cu substrates covered with catalytic inactive oxides<sup>17,18</sup> or decorated with nanoparticles as preseeded nucleation sites,<sup>19</sup> were reported to lower the nucleation density to  $\leq 100$  nuclei/cm<sup>2</sup>. Graphene single crystals with submillimeter to millimeter sizes can now be obtained with these reaction recipes, despite harsh synthetic conditions being involved, e.g., high annealing pressure (~2 atm),<sup>16</sup> elevated temperature (1100 °C),<sup>15</sup> extended annealing period (>3–7 h),<sup>16,20</sup> and prolonged growth time (6–48 h).<sup>17</sup> Recently, a small one-end open quartz tube (of about a half inch in diameter) was introduced into a conventional CVD tube furnace for reactant vapor trapping, which allowed the modulations of both gas compositions and gas flow rates within the small tube. Consequently, a successful enlargement of graphene single crystals up to 100 μm was achieved without applying harsh synthetic conditions.<sup>21</sup> With the similar strategy, a circumfluence CVD reaction was reported to achieve ultralow density of ~10 nuclei/cm<sup>2</sup>. However, a broad distribution of nucleation densities, ranging from 30 000 to 10 nuclei/cm<sup>2</sup>, was

Received: April 19, 2015

Revised: August 28, 2015

Published: September 1, 2015

observed along the entire catalytic Cu substrate from the end nearby the gas inlet to the other end of the gas outlet.<sup>22</sup> Herein, we report an alternative approach to preparing large-area graphene single crystals using a specifically designed LPCVD reactor with confined reaction space (L 22 mm  $\times$  W 13 mm  $\times$  H 50  $\mu$ m). Within the confined reaction space, a uniform distribution of reactant concentrations and reduced substrate roughness, as well as the shift of growth kinetics toward a diffusion-limited regime, can be achieved, favoring the preparation of large-area, high-quality graphene single crystals. With this reactor configuration, we were able to prepare submillimeter graphene grains ( $\sim$ 0.8 mm) under conventional synthesis temperature (1050  $^{\circ}$ C) and low chamber pressure ( $\leq$ 2 Torr) within a reasonable time lapse ( $\leq$ 5 h).

## EXPERIMENTAL SECTION

**Catalytic Growth of Graphene.** The catalyst-assisted syntheses of graphene single crystals were carried out in an LPCVD system with a 25- $\mu$ m-thick Cu foil (Alfa Aesar, purity 99.8%) placed in the 10-cm-long heating zone of a tubular furnace (Thermo Scientific, Lindberg/Blue M). To grow large-area graphene single crystals, a few LPCVD reactors with various configurations designed to accommodate the catalytic Cu substrate were tested. An optimal configuration containing a confined reaction room (L 22 mm  $\times$  W 13 mm  $\times$  H 50  $\mu$ m) in the synthesis reactor to locate the 25- $\mu$ m-thick Cu foil was finally selected to systematically examine the synthesis protocols (as listed in Table S1), including reaction temperature, chamber pressure, flow rates, and reaction precursor compositions during the annealing and growing periods in the LPCVD reaction. Details of the catalytic growth of graphene are described in Section 1 of the Supporting Information.

**Raman Characterization and Mapping.** The graphene domains transferred on a SiO<sub>2</sub>/Si substrate were characterized by micro-Raman microscopy (NT-MDT, NTEGRA) with a semiconductor laser (Sapphire, 488 FP) of  $\sim$ 80 mW at 488 nm as an excitation source. A 100 $\times$  objective was used to focus the laser beam onto the graphene sample with a spot size of  $\sim$ 1  $\mu$ m<sup>2</sup>. Signals with the Raman shifts from 1200 to 3500 cm<sup>-1</sup> were collected with a CCD camera (Andor Technology, DV401) integrated into the NTEGRA spectral system. The characteristic peak of the Si substrate at 521 cm<sup>-1</sup> was utilized as an internal standard to calibrate the relative spectral intensities. Raman mapping was conducted by raster scanning the laser spot over a selected area of the sample surface with a step size of 0.5  $\mu$ m and an exposure time of 0.5 s at each imaging point.

**Electron Microscopy Characterization.** Filed-emission scanning electron microscopy (FE-SEM, JEOL, JSM-7600F) operated at an acceleration voltage of 5 kV and high-resolution transmission electron microscopy (HR-TEM, FEI Tecnai G2 20 LaB6) operated at 160 kV were utilized to characterize the morphology and crystal structure of the as-synthesized graphene domains. From the SEM images, fine structures such as wrinkles and dendritic shapes of graphene domains can be observed, providing additional information about morphological variations of the as-synthesized graphene. The crystallinity of a graphene grain was characterized by examining the angle shifts of individual selective-area electron diffraction (SAED) patterns recorded at different positions across the graphene domain of interest.

### Simulation of the Flow Field in Confined Reaction Space.

The gas flow pattern plays a significant role for the thin-film deposition in CVD reactions. In this study, we employed the finite element method (FEM) simulation to examine the gas flow pattern within a confined reaction room for graphene synthesis in the LPCVD reaction (see also Section 5 of the Supporting Information). Numerical results of the gas flow field and reactant mass transport computed from the FEM simulation provide insight into the transport of reactants within the confined reaction space for the effective growth of large-area, single-crystal graphene.

## RESULTS AND DISCUSSION

As illustrated in Figure 1a and Figure S1 of the Supporting Information, a rectangular reactor with confined space located

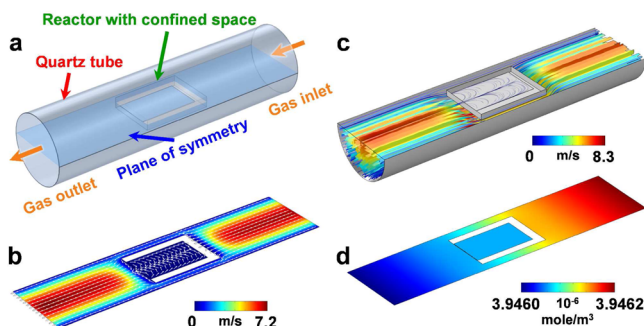


**Figure 1.** Illustration of an LPCVD reactor and computational results of the FEM simulation. (a) Schematic of the 10-cm-long heating zone of a tubular furnace utilized for graphene synthesis. Located in the central heating zone is a reactor with confined space (L 22 mm  $\times$  W 13 mm  $\times$  H 50  $\mu$ m) to accommodate a 25- $\mu$ m-thick Cu foil. On the plane of symmetry, flow areas that reacting gases can reach are marked in blue. (b) Computational result from the FEM simulation manifests the flow velocity on the plane of symmetry where white arrows exhibit the transport direction of reactants flow. (c) The transport of reactants flow is represented by the streamlines colored by flow speeds with their widths proportional to the cell Reynolds number, which defines the relative ratio of convective to diffusive fluxes. (d) The simulated concentration distribution of reactants on the plane of symmetry.

in the 10-cm-long heating zone of a quartz tubular LPCVD system was applied for the graphene synthesis. The strategy of using this space-confined configuration to reduce the nucleation density for preparing large-area graphene single crystals was confirmed by comparing three reactors with different designs (Figure 2a–c). In a conventional CVD experimental setup (Figure 2a), the catalytic Cu foil was placed on a tungsten (W) boat with its front side exposed directly to reacting precursors. After synthesis, the Cu substrate with grown graphene grains was oxidized on an ambient hot plate, where the Cu surface covered with graphene was oxidation resistant, rendering the synthesized graphene grains easily identified by the color contrast of an optical micrograph (Section 2 of the Supporting Information).<sup>23</sup> We found that the graphene growth rates on both sides of the Cu substrate are different. With the synthetic protocol of P1 (as listed in Table S1 of the Supporting Information) adopted in the reaction, the front Cu surface (Figure 2g), which is almost fully covered with graphene grains, displayed a much higher growth rate compared to the rear Cu surface (Figure 2d). This outcome was attributed to the difference in the mass-transport rates of carbon species through the boundary (stagnant) layer in the vicinity of the Cu surface and can be explained with a conventional kinetic model for the thin-film deposition in a CVD reaction. The growth kinetics involves the competition between the mass-transport (diffusion) and surface-reaction (edge-attachment) processes. For the mass-transport process, the synthesis/deposition rate is governed by mass transport coefficient of  $h_g = D_g/\delta$ , where  $D_g$  is the gas diffusion coefficient and  $\delta$  is the boundary layer thickness. In contrast, graphene deposition through the surface-reaction processes is proportional to the surface reaction constant ( $k_s$ ), which increases exponentially with the reaction temperature.<sup>24</sup>

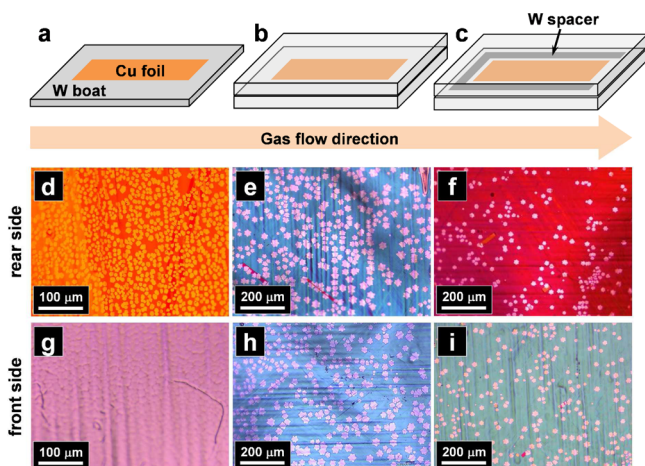


**Figure 2.** Illustrations of three reactor configurations and optical micrographs of the as-synthesized graphene. (a) The Cu substrate placed on a tungsten (W) boat is exposed to gaseous reactants directly. (b) The Cu substrate is sandwiched between two quartz slides. (c) A tungsten (W) spacer is placed between two quartz slides to prevent their coalescence with the Cu substrate and to create a confined reaction space. (d–i) Optical micrographs of the as-grown graphene on the rear (d–f) and front (g–i) sides of the catalytic Cu substrate. Enlarged optical micrographs of parts d–f are shown in Figure S3 for easier comparison of the graphene-shape transformation due to different growth-controlling mechanisms, i.e., surface-reaction (edge-attachment) versus mass-transport (diffusion).

According to the Blasius model, the thickness of the laminar boundary layer ( $\delta$ ) is inversely proportional to the square root of the reactant's flow velocity.<sup>25</sup> Compared with the front Cu surface (Figure 2g), which experienced a higher flow rate, the rear Cu surface (Figure 2d) was subjected to a much slower gas flow due to the reduced interface between the Cu surface and the tungsten boat (Figure 2a). The decreased flow velocity therefore induced a thicker boundary layer, thus reducing the mass transport efficiency ( $h_g = D_g/\delta$ ) of carbon deposition onto the rear Cu surface and leading to the final decrease of graphene growth. Therefore, the observed difference in the growth rates on different sides of the Cu substrate demonstrates the unequivocal effect of mass-transport process on the graphene synthesis. Furthermore, the shape of the generated graphene grains contains a compact structure with sharp edges (Figure 2d and an enlarged image in Figure S3a), which was considered as a result of the edge-attachment-limited growth, implying that the surface-reaction process also took part in the growth reaction.<sup>12,26</sup> Therefore, using the protocol P1 in the reactor configuration of Figure 2a, the synthesis kinetics falls into the region where both the mass-transport and surface-reaction processes were involved in the graphene growth.

The growth of large-area graphene single crystals can be manipulated judiciously by shifting the synthesis kinetics from surface-reaction (edge-attachment)-limited to mass-transport (diffusion)-limited regimes via the introduction of oxygen to the CVD reaction.<sup>12,17</sup> Inspired by these pioneering studies and our own observation from Figure 2d that the mass-transport (diffusion) process becomes noticeable under reduced gas flow, we proposed to guide the graphene growth by significantly suppressing the local flow of reactants on the Cu surface. To this end, a confined reaction space was delicately designed, where the Cu foil was sandwiched by a pair of quartz slides and

secured with a tungsten clamp (Figure 2b). With this setup and the synthesis protocol of P2 (Table S1, which differs from P1 only by reaction time), the graphene grains grown on both sides of Cu were found to have similar size, coverage, and nucleation density (Figure 2e,h). In addition, within the confined space, the sublimation and redeposition of Cu atoms tended to reach equilibrium, leading to the significant suppression of surface roughness on the catalytic Cu substrate<sup>13,14</sup> and the consequent facilitation of reducing nucleation density.<sup>14</sup> Comparing the nucleation densities, the sandwiched configuration ( $\sim 6.8 \times 10^4$  nuclei/cm<sup>2</sup>, Figure 2e) has improved the conventional setup ( $\sim 9.6 \times 10^5$  nuclei/cm<sup>2</sup>, Figure 2d) by 14-fold. Furthermore, the gas flow velocity on the Cu surface in the sandwiched configuration was reduced significantly, resulting in a thick boundary layer extending over the space between the Cu surface and quartz slides (Section 6 of the Supporting Information). Consequently, the diffusion transport of carbon flux through the boundary layer to the substrate surface becomes dominant in the graphene synthesis, which was confirmed by the shape transformation of graphene grains toward a multibranch or dendritic structure (Figure 2e and an enlarged image in Figure S3b), which is a hallmark of mass-transport (diffusion)-limited growth.<sup>12,27,28</sup> The lack of high velocity bulk flow in the confined space provided an additional advantage: Collision-desorbed carbon species failed to escape easily from the catalytic Cu surface and were prone to incorporate into the existing carbon clusters, eventually improving the enlargement of graphene grains within a reasonable reaction time.<sup>29</sup>

However, parts of the Cu substrate melted at elevated temperature to coalesce with the reactor (Figure S4), making it difficult to remove the as-grown graphene/Cu substrate from the quartz slides after the reaction for further optical characterization and device fabrication. Therefore, we modified the design by introducing a U-shaped tungsten spacer (50  $\mu\text{m}$  in height) between the quartz slides to create a tiny, but sufficient, reaction room to accommodate a 25- $\mu\text{m}$ -thick Cu foil (Figure 2c), where the gas inlet was oriented toward tailwind to prevent the direct injection of gas flow. With this setup, the nucleation density was further reduced ( $\sim 4.7 \times 10^4$  nuclei/cm<sup>2</sup> in Figure 2f,i and an enlarged image in Figure S3c) in the CVD reaction, where the required reactants (P3 in Table S1) could be diluted substantially, and the coalescence of Cu foil with quartz slides was finally avoided. To find an optimal gap dimension (i.e., the spacer height) of the confined reaction room, various gap sizes (50, 100, 180, 300, and 500  $\mu\text{m}$ ) of the reactor were examined. With the same synthesis protocol (Table S1, P13) tested, the resultant nucleation density decreases monotonically with the reduction of gap size (Figure S5). Since the confined space with a gap of <50  $\mu\text{m}$  to accommodate a 25- $\mu\text{m}$ -thick catalytic Cu foil could cause the coalescence of a melted copper foil with the reactor, the tested reactors with a spacer of 50  $\mu\text{m}$  in height were utilized for the rest of the experiments. In addition, the study of gap-size effect clearly demonstrates the controllable scalability of the reactor reported here. The gap size of the reactor can be easily adjusted for the Cu foils of different thickness to achieve the best synthesis condition. It can also be expected that the lateral dimensions (length and width) of the reactor can be expanded to accommodate a large Cu substrate. Moreover, multiple reactors can be piled up and applied simultaneously in a CVD reaction to facilitate a high production throughput.

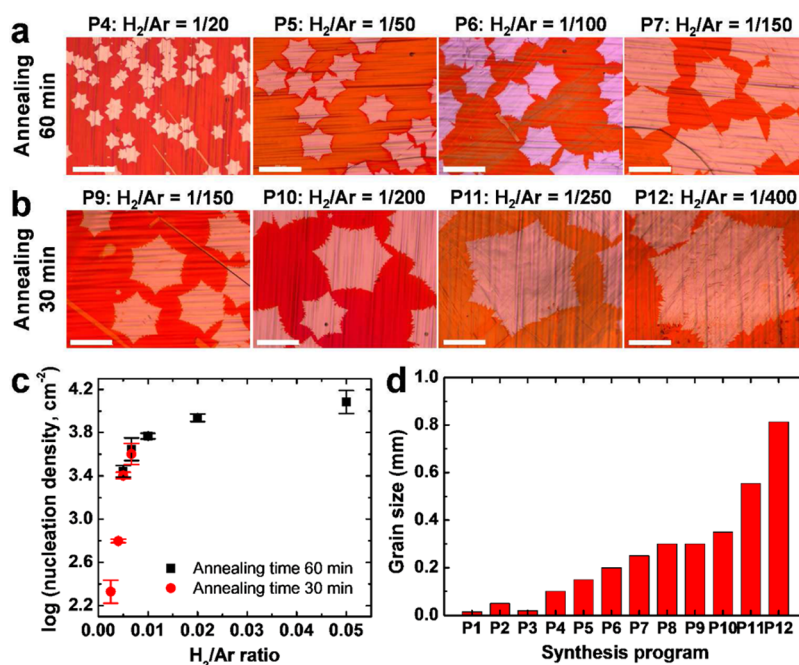


**Figure 3.** Effects of H<sub>2</sub> concentration on the nucleation density. (a) With the same reaction temperature, reacting precursors, and chamber pressure, the reduced H<sub>2</sub>/Ar ratio during annealing (for 60 min) assists the decrease of nucleation density. Scale bars: 200  $\mu\text{m}$ . (b) Additional decrease of the H<sub>2</sub>/Ar ratio with the concomitant reduction of exposure time (down to 30 min) to H<sub>2</sub>/Ar further lessens the nucleation density, rendering the growth of larger graphene grains. Scale bars: 200  $\mu\text{m}$ . (c) The measured nucleation density as a function of H<sub>2</sub> concentration and exposure time to H<sub>2</sub>/Ar. A low density of  $\sim 200$  nuclei/cm<sup>2</sup> can be achieved by reducing H<sub>2</sub> concentration (from H<sub>2</sub>/Ar ratio of 0.05 to 0.0025) and shortening the exposure time (30 min) to H<sub>2</sub>/Ar during annealing. (d) Graphene domains of various sizes were obtained from different synthesis protocols (as listed in Table S1). Single-crystal graphene of  $\sim 0.8$  mm in diagonal diameter can be prepared with the optimal synthesis protocols.

To verify the advantage of using this confined reaction room (Figure 2c) for large-area graphene synthesis, numerical FEM simulation was employed to unveil the gas flow field in the CVD reaction. The geometry utilized to simulate the CVD system is illustrated in Figure S1a with a tailwind gas inlet of reacting precursors. In the 10-cm-long central heating region of the tubular furnace (Figure 1a) where graphene synthesis occurs, the simulation results (Figure 1b) show that the extremely low gas flow velocity ( $2.5 \times 10^{-12}$  m/s) within the confined reaction room was reduced by >10 orders of magnitude compared to the bulk flow rate (7.2 m/s) outside of the confined space. The white U-shaped area without velocity distribution indicates the location of the tungsten spacer, which defined the dimension of the confined reaction room. Inside the confined reaction room (Figure 1b), white arrows indicate the transport of reactants that flow in along the sidewalls and circulate out from the central axial region of the confined space. The simulation also confirms our expectation that the gas flow within the confined space significantly reduces; meanwhile, the thickness of the boundary layer on catalytic Cu surface increases extensively to cover the whole space between the Cu surface and quartz slides (Section 6 of the Supporting Information). Consequently, the mass transport of reactants onto the catalytic Cu substrate is effectively reduced, leading the growth kinetics toward the mass-transport-limited regime. Figure 1c provides a comprehensive map of the reactant flow, where the streamlines are colored by flow speeds with their widths proportional to the cell Reynolds number. The cell Reynolds number is considered as the Péclet number that defines the relative ratio of convective to diffusive fluxes across the unit simulation cell.<sup>30</sup> Narrow lines hence signify diffusion-dominant flows, to which the majority within the

confined space belongs, rendering a homogeneous distribution of the reactants in the reaction room (Figure 1d). From these simulations, we prove that the reduced flow velocity, diffusion-dominant mass transport, and homogeneous distribution of reactants in the confined CVD reaction space benefit the preparation of large-area graphene single crystals. Furthermore, to demonstrate the scalability of the CVD method with a space-confined reactor adopted in this study, we performed a simulation for the reaction system composed of a large tube furnace (Figure S6a–c, 20.32 cm in diameter and 120 cm in length) with an amplified rectangular reactor (Figure S6d, L 20 cm  $\times$  W 14.4 cm  $\times$  H 4 mm with a confined reaction room of L 17.6 cm  $\times$  W 10.4 cm  $\times$  H 50  $\mu\text{m}$ ). To facilitate an efficient computation, the geometry of the reaction system was divided into five different domains with appropriate mesh resolutions (Figure S6e). The simulation of this enlarged CVD system (Figure S6f–h) confirmed that the fluid conditions, including reduced flow velocity, diffusion-dominant fluxes, and a homogeneous reactant distribution, are similar to those (Figure 1) of the chamber/reactor with much smaller dimensions, demonstrating the scalability of this space-confined reactor for the synthesis of large-area graphene single crystals.

Adopting the setup shown in Figure 2c, we focused on testing the synthesis parameters to further reduce the nucleation density. First, we adjusted the H<sub>2</sub> concentration during annealing in the graphene synthesis (Figure S2). It is known that annealing the Cu substrate in the presence of H<sub>2</sub> helps to remove contaminations and oxides on Cu, thus providing a clean, active catalytic surface for graphene growth. However, an overactive surface could cause the increase of nucleation density, which is ultimately detrimental to growing large graphene grains. Therefore, we treated the Cu substrate

with acetic acid to partially remove contaminations and oxides on Cu to reduce the gas amount and exposure time of H<sub>2</sub> required during the annealing. From the measurements, we found that the nucleation density could be effectively lowered by reducing the H<sub>2</sub>/Ar ratio (Figure 3a,b) and shortening the exposure time to H<sub>2</sub> during the annealing (Figure S7). Nucleation densities formed as a function of reacting H<sub>2</sub> concentration in combination with annealing time, where the nucleation density decreases monotonically by ~100-fold upon reducing the H<sub>2</sub> concentration, are summarized in Figure 3c. As a result, a nucleation density of ~200 nuclei/cm<sup>2</sup> concomitant with the consequent growth of graphene grains of ~0.8 mm in diameter were achieved (Figures 3d and S8).

In addition to the optical imaging, SEM characterization was applied to examine the morphology of the as-synthesized graphene. With the optimized synthesis protocol (Table S1, P12), large graphene domains with similar sizes (~0.8 mm in diagonal diameter) developed from ~6 distinct nuclei were identified in an area of 3.1 mm<sup>2</sup> (i.e., ~200 nuclei/cm<sup>2</sup>, Figure 4a). To obtain isolated graphene single crystals, the growth

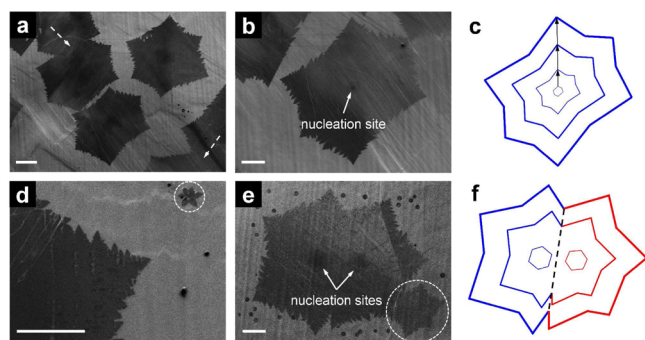


**Figure 4.** (a, b, d, e) SEM images were used for detailed investigations of the size and morphology of the as-synthesized graphene samples on Cu substrates. The extension process of a representative single-crystal graphene grain shown in (b) is illustrated in (c), where black arrows depict the growth direction of a lobe. Occasionally, small graphene grains, marked with the white-dashed circles in (d) and (e), were found nearby the pre-existing large domains. (e) A large polygonal graphene grain composed of two patches, which was developed from distinct nuclei, was also observed. (f) The peripheries of these constituent graphene grains are indicated with different colors, where the black-dashed line indicates the location of a grain boundary. The small black spots on the Cu substrate in (e) came from the oil vapor contamination, unintentionally introduced during the sample storage. Scale bars: (a) 200  $\mu\text{m}$  and (b, d, e) 100  $\mu\text{m}$ .

reaction was ceased in 270 min to prevent the conjunction of neighboring grains; nevertheless, some coalescences between graphene domains did occur at the areas indicated with the white-dashed arrows in Figure 4a. Occasionally, small graphene grains (marked with the dashed circles in Figures 4d,e) were found nearby and tended to merge with the pre-existing large domain, resulting in polycrystalline films. Typically, the isolated graphene grains prepared in this study were developed from single nucleation sites and displayed a symmetric six-lobe geometry of clear dendritic structures at the edge (Figure 4b). Figure 4c illustrates the extension process of an isolated graphene grain shown in Figure 4b, which is regarded as a single crystal of slightly anisotropic growth introduced by the crystal direction of the underlying Cu substrate.<sup>31</sup> Additionally, large graphene grains with a polygonal (more than six lobes) geometry were also observed. As shown in Figure 4e, two

distinct nucleation sites were identified in a large graphene grain, demonstrating that this large polygonal domain consisted of two patches developed from different nuclei. In Figure 4f, enlargement of the peripheries of constituent graphene grains are indicated with different colors to illustrate how these two patches merge to form a large domain. The black-dashed line in Figure 4f indicates schematically the location of a grain boundary. Recently, practical geometric models have been reported to effectively describe the dynamic formation of grain boundaries, resulting from the coalescence of hexagonal graphene grains with straight edges.<sup>32</sup> Comparatively, the structure of grain boundaries formed by graphene grains with dendritic lobes is more complicated and requires the HR-TEM images with atomic resolution to determine its actual distribution.

The as-synthesized graphene on the Cu surface was then transferred onto a receiving Si wafer (i.e., SiO<sub>2</sub>/Si substrate) for further optical and electrical characterizations (Section 3 of the Supporting Information). Figure 5a shows the optical image of a graphene grain of 0.45 mm in diagonal diameter, of which the Raman spectroscopic recording was conducted to characterize its layer number, structural defect, and sheet quality. In Figure 5b, Raman-scattering signals observed at seven randomly selected positions on the graphene grain (Figure 5a) demonstrate their excellent spectral consistency, indicating the uniformity of the as-synthesized graphene. Moreover, judging from the negligible D-band intensity at ~1350 cm<sup>-1</sup>, no apparent defects in the graphene grain were observed. The positions and relative intensities of G (~1572 cm<sup>-1</sup>) and 2D (~2684 cm<sup>-1</sup>) bands also agree with those of the monolayer graphene reported previously.<sup>33–36</sup> In addition, two-dimensional Raman mapping over a selected area, marked by a red-dashed square in Figure 5a, was performed to examine the spatial uniformity. The obtained Raman mappings of 2D, G, and D bands together with the 2D bandwidth (fwhm: full width at half-maximum), 2D peak position, and the intensity ratio of  $I_{2D}/I_G$  are displayed in Figure 5c–e and Figure S9a–c, respectively. While the dendritic structure of grain edges and the wrinkle distribution in the 2D and G band mappings (Figure 5c,d) are recognized, the extremely low intensity of the D band over the whole mapping area (Figure 5e) again indicates the high uniformity and defect-free properties in the as-synthesized graphene. Figure 5f–h summarizes the narrowly distributed histograms, analyzed from the mappings of Figure S9a–c, to yield the 2D fwhm of  $34.0 \pm 2.4 \text{ cm}^{-1}$ , 2D peak position of  $2684.5 \pm 3.7 \text{ cm}^{-1}$ , and  $I_{2D}/I_G$  of  $3.9 \pm 0.7$  (where  $I_{2D}/I_G > 3$  for >93% data points), which further support a uniform monolayer of the as-synthesized graphene.<sup>33–36</sup>

The crystallinity of the as-synthesized graphene was examined by normal-incident selective-area electron diffraction (SAED) from nine randomly selected locations (the labeled red spots of c–k in Figure 6a with the separation of >50  $\mu\text{m}$  among these spots) on a graphene grain (~0.35 mm in diameter) to display a typical 6-fold symmetry (Figure 6c–k).<sup>37</sup> The representative line profile of the diffraction peak intensities (Figure 6b) along the white arrows shown in Figure 6c indicates that the {1100} spots are more intense than the {2110} spots with  $I_{\{1100\}}/I_{\{2110\}} \sim 1.1$ , supporting the monolayer characteristic of graphene.<sup>38,39</sup> The graphene lattice orientation, defined by the angle ( $\theta$ ) between [1010] and the x-axis (Figure 6d), is extracted from individual SAED patterns, where a rotation less than 1.4° was observed for the lattice

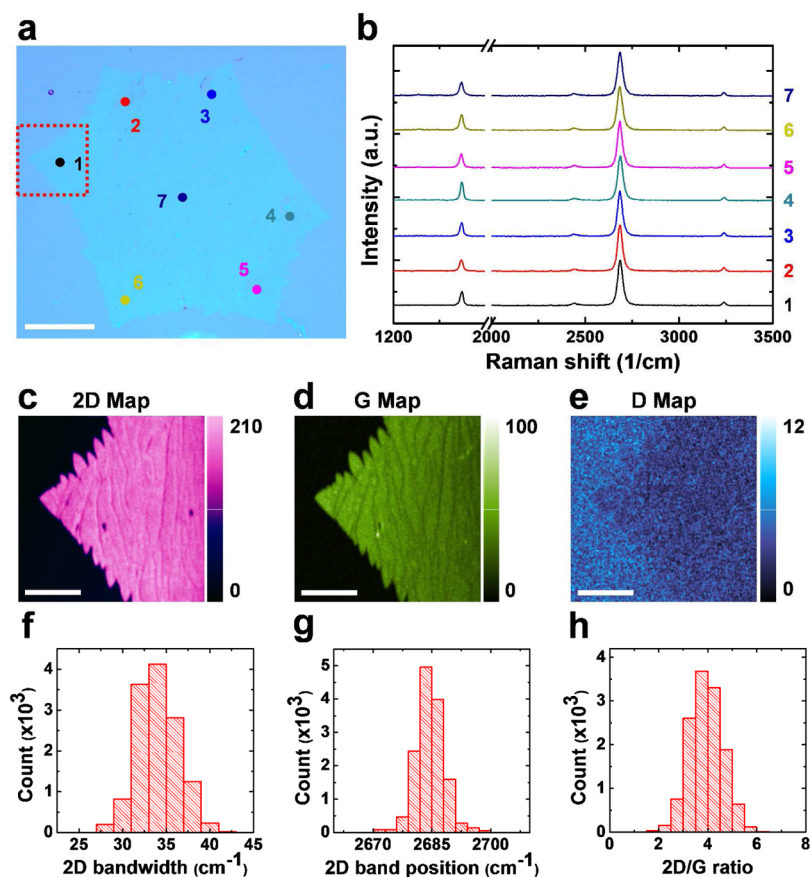


**Figure 5.** Raman characterization/mapping of the as-grown graphene. (a) Optical image of the as-grown graphene of 0.45 mm in diameter after it was transferred to a Si wafer from the catalytic Cu surface. Scale bar: 100  $\mu\text{m}$ . (b) Raman spectra were recorded at seven spots, as indicated in (a) on the transferred graphene grain. (c–e) Raman intensity mappings of the 2D, G, and D bands of graphene in the selected area marked by a red-dashed square in (a). Scale bars: 30  $\mu\text{m}$ . (f–h) Histograms summarized from the Raman mappings of (f) 2D bandwidth (fwhm), (g) 2D peak position, and (h) the intensity ratio of  $I_{2D}/I_G$ .

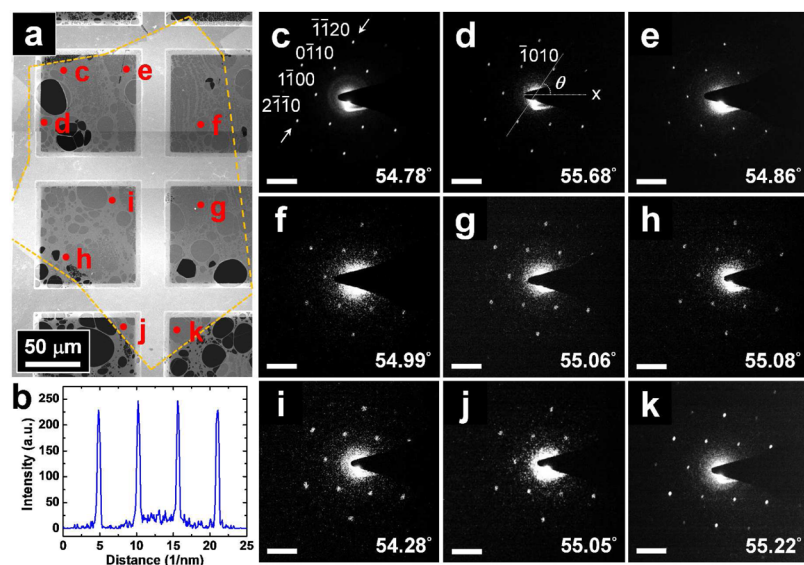


**Figure 6.** (a) SEM image of a graphene grain of  $\sim 0.35$  mm in diameter (with its contour marked by yellow-dashed lines) on a Lacey carbon-coated Cu grid for TEM examination. (b) A line profile of the diffraction peak intensities along the white arrows indicated in (c). (c–k) SAED patterns recorded from different locations on the graphene grain, as labeled by red spots in (a). The graphene lattice orientation, defined with an angle ( $\theta$ ), is extracted from each SAED pattern and gives a rotation less than  $1.4^\circ$ . Scale bars: 5  $\text{nm}^{-1}$ .

orientation of the graphene grain under study, once more manifesting its single crystalline nature.

Finally, the electrical transport properties of a graphene-based field-effect transistor (called graphene-FET) were

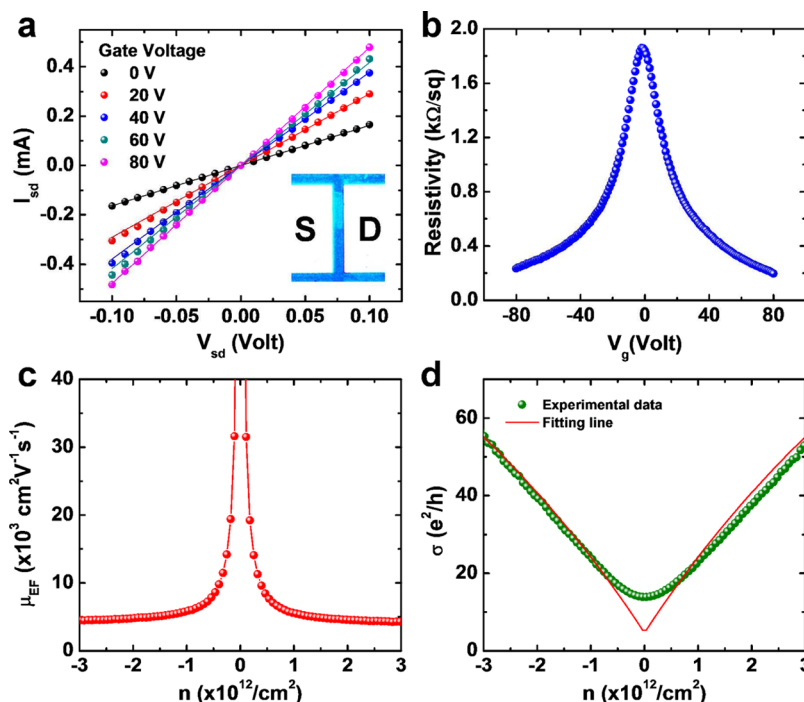


**Figure 7.** Electrical transport of the as-synthesized graphene. (a) The  $I_{sd}$ – $V_{sd}$  curves of the as-fabricated graphene–FET device measured at various  $V_g$  values. The inset shows the optical micrograph of a representative graphene–FET device (S: source and D: drain) with a conducting channel of  $24 \times 8 \mu\text{m}^2$ . (b) Channel resistivity of the graphene–FET device is plotted as a function of  $V_g$ . (c) The variation of  $\mu_{EF}$  with respect to  $n$  is deduced from the experimental data. (d) The  $\sigma$  of the as-fabricated graphene–FET is plotted as a function of  $n$ , where a self-consistent diffusive transport model (red solid line) was applied to fit the experimental data (green spheres).

characterized by conducting the source–drain current vs source–drain voltage ( $I_{sd}$ – $V_{sd}$ ) and source–drain current vs gate voltage ( $I_{sd}$ – $V_g$ ) measurements, where the device fabrication and electrical measurements of graphene–FETs are described in Section 4 of the Supporting Information. In Figure 7a, the linear  $I_{sd}$ – $V_{sd}$  curves recorded at various  $V_g$  values indicate a good ohmic contact between the graphene channel and Cr (10 nm)/Au (50 nm) electrodes. The device resistance ( $R_{tot} = V_{sd}/I_{sd}$ ) is a combination of the metal/graphene contact resistance ( $R_{contact}$ ) and the graphene channel resistance ( $R_{channel}$ ). The  $R_{contact}$  was determined from a fit to experimental data (Section 4 of the Supporting Information) to be  $\sim 194 \Omega$ , which was then subtracted from  $R_{tot}$  to enable the direct evaluation of channel resistivity ( $\rho = R_{channel} \times (W/L)$ ;  $W$ , channel width;  $L$ , channel length) as a function of  $V_g$  (Figure 7b). As a result, the low resistivity of  $\rho \sim 230 \Omega/\text{sq}$  at high  $V_g$  and the peak resistivity of  $\sim 1.9 \text{ k}\Omega/\text{sq}$  at the Dirac point ( $V_{Dirac} = -1.5 \text{ V}$ ) were obtained, rendering an on/off ratio of  $\sim 8$ . The nonzero  $V_{Dirac}$  value implies an unintentional charged doping on the graphene film.

Figure 7c shows the field-effect mobility ( $\mu_{EF} = 1/nep$ ;  $n$ , carrier density;  $e$ , elementary charge)<sup>40,41</sup> as a function of  $n$ , which can be calculated from  $n = C_g(V_g - V_{Dirac})/e$  with  $C_g = 11.5 \text{ nF}/\text{cm}^2$  being the capacitance for the 300 nm-thick  $\text{SiO}_2$  dielectric layer.<sup>42</sup> The recorded data demonstrate that  $\mu_{EF} > 8300 \text{ cm}^2 \text{ V}^{-1} \text{ s}^{-1}$  at  $n < 5 \times 10^{11} \text{ cm}^{-2}$  and a limit of  $\mu_{EF} \sim 4800 \text{ cm}^2 \text{ V}^{-1} \text{ s}^{-1}$  is achieved at  $n = 3 \times 10^{12} \text{ cm}^{-2}$ . The electrical conductivity ( $\sigma$ ) defined by the self-consistent diffusive transport model gives  $\sigma^{-1} = (ne\mu_c + \sigma_0)^{-1} + \rho_s$ <sup>43,44</sup> where  $\mu_c$  refers to the carrier-density-independent mobility corresponding to the Coulomb long-range scattering by charged impurities,  $\sigma_0$  is the residual conductivity at the Dirac point, and  $\rho_s$  is the resistivity associated with short-range

scattering due to the lattice defects of graphene.<sup>45</sup> The  $\sigma$ – $n$  fit in Figure 7d yields  $\mu_c \sim 5300 \text{ cm}^2 \text{ V}^{-1} \text{ s}^{-1}$ , which is of medium value among those of the synthesized single-crystal graphene reported.<sup>12–14,16,17,22,46,47</sup> We also found that the recorded minimum conductivity ( $\sigma_{min} \sim 13.8 e^2/h$ ) is higher than  $4 e^2/h$  of a perfect graphene, which is likely due to the inhomogeneous distribution of charged impurities on graphene.<sup>42</sup> Both nonzero  $V_{Dirac}$  and deviated  $\sigma_{min}$  imply the degraded mobility of our single-crystal graphene; therefore, reducing charged impurities by modifying the surface of the  $\text{SiO}_2/\text{Si}$  substrate and developing a residue-free transfer process in the sample preparation should substantially improve the electric transport in graphene.

In addition, taking advantage of the large graphene domains obtained in this study, we examined the length-dependence of the field-effect mobility in graphene devices on the channel length ( $L_{ch}$ ) ranging from 8 to 560  $\mu\text{m}$ , where the channel width ( $W_{ch}$ ) was maintained to be  $>50 \mu\text{m}$  to minimize the effect of width-dependent mobility.<sup>48</sup> From Figure S10, it is found that the device mobility increases as extending the channel length and tends to level off at a large channel length. This result is consistent with previously reported studies<sup>48–50</sup> and further confirms the highly uniform quality of the as-synthesized graphene crystals across large distance scales. The sheet resistance of a continuous graphene film is another significant electrical metric to evaluate the performance of graphene samples, especially for the application as an electrode material in optoelectronic devices.<sup>51</sup> In this study, two different types of continuous graphene films were synthesized; one was obtained with a conventional method (Figure 2a, composed of multiple small graphene grains of  $<50 \mu\text{m}$  in diameter, synthesized with P1 in Table S1 and a growth time of  $\sim 50$  min to ensure a complete conjunction of individual grains on

both sides of the Cu substrate) and the other was prepared in the confined reaction room (Figure 2c, composed of multiple large graphene single crystals of  $>500\ \mu\text{m}$  in diameter, synthesized with P12 in Table S1 and a growth time of  $\sim 6\ \text{h}$  to ensure a complete conjunction of individual grains). The sheet resistances were measured using a conventional four-point probe method with a Keithley 2400 multimeter. Representative sheet resistances of the pristine CVD-synthesized monolayer graphene films obtained by other research groups together with ours of this study are summarized in Figure S11. It is obvious that the continuous graphene films composed of large graphene single crystals ( $171.9 \pm 87.4\ \Omega/\text{sq}$ ) possess much smaller sheet resistances than those films that consist of small graphene grains ( $367.7 \pm 120.5\ \Omega/\text{sq}$ ). The measured sheet resistances are comparable to those of several other representative studies as shown in Figure S11.

To compare with previously reported studies, a list of the performance parameters of representative protocols for synthesizing large graphene single crystals is summarized in Table S2. Except the works reported by the Ruoff's group,<sup>12,14</sup> our study shows improvements in some of the following aspects, including crystal size, the duration of a complete synthesis cycle, required working temperature, and the electrical properties of graphene, as compared to most of the previous studies. Furthermore, although the growth rate in this study is moderate, our method provides a favorable duration for a complete synthesis cycle (including the annealing and growth periods) that determines the ultimate throughput of graphene production. Another advantage of this method is to preclude the contamination of  $\text{SiO}_2$  nanoparticles on the graphene surface (Figure S12), which is an issue frequently encountered in the graphene synthesis without an effective solution.<sup>52–54</sup> The  $\text{SiO}_2$  contamination stemmed from the  $\text{H}_2$  etching of a quartz tube in the CVD synthesis of graphene at high reaction temperature ( $>800\ ^\circ\text{C}$ ).<sup>52</sup> In contrast, with the Cu substrate located in the confined reaction room of this study, the  $\text{SiO}_2$  contamination can be substantially excluded (Figure S12c,d). Within the confined reaction room, the very narrow gas inlet results in the extremely slow gas flow, which effectively prevents the entry of  $\text{SiO}_2$  nanoparticles carried by the reactant flow and also assists the reduction of reactive  $\text{H}_2$  to etch the quartz walls of the space-confined reactor.

## CONCLUSION

In conclusion, we report a convenient, facile method to prepare high-quality graphene single crystals through the novel design of a CVD reactor with a confined reaction space. The space-confined configuration for synthetic reactions reported here (at synthesis temperature  $1050\ ^\circ\text{C}$ , chamber pressure  $\leq 2\ \text{Torr}$ , and reaction time  $\leq 5\ \text{h}$ ) provided multiple advantages for the preparation of large graphene single crystals by suppressing the substrate roughness, establishing a uniform distribution of reactant concentrations, and shifting the growth kinetics toward a diffusion-controlled reaction. Numerical FEM simulations provided insight into the transport of reactants within the confined reaction space and further supported our experimental observations. From the simulations, a homogeneous reactant distribution was established within the confined space, where the diffusion transport of reactants through the boundary layer became the rate-determining step of graphene deposition. Using the space-confined reactor together with the optimized synthesis parameters by reducing both the exposure time and gas amount of  $\text{H}_2$  during annealing enabled the growth of

graphene single crystals up to  $\sim 0.8\ \text{mm}$  in diameter. The as-synthesized graphene was characterized to be monolayer, high uniformity, and low defects with  $\mu_{\text{EF}} \sim 4800\ \text{cm}^2\ \text{V}^{-1}\ \text{s}^{-1}$  at room temperature. The method reported here provides an alternative approach to prepare submillimeter graphene single crystals without involving harsh synthetic conditions, such as prolonged growth time (6–24 h), escalated chamber pressure ( $\sim 2\ \text{atm}$ ), and high concentration ( $>99\%$ ) of explosive  $\text{H}_2$ . Finally, as supported by the FEM simulation of both small and enlarged CVD systems, the structural design of the CVD system by adjusting the space-confined reactor's dimensions is of facile controllability and scalability, demonstrating the superiority and preference of this method for practical and industrial applications in the future.

## ASSOCIATED CONTENT

### Supporting Information

The Supporting Information is available free of charge on the ACS Publications website at DOI: [10.1021/acs.chemmater.5b01430](https://doi.org/10.1021/acs.chemmater.5b01430).

Experimental details of preparing monolayer, single-crystal graphene: catalytic growth, thin-film transfer, device fabrication, electrical measurement, FEM simulation, Tables S1–S2 of synthesis protocols, and Figures S1–S12 (PDF)

## AUTHOR INFORMATION

### Corresponding Authors

\*(C.-C.C.) E-mail: [chencc@mail.tku.edu.tw](mailto:chencc@mail.tku.edu.tw).

\*(Y.-T.C.) E-mail: [ytccchem@ntu.edu.tw](mailto:ytccchem@ntu.edu.tw).

### Notes

The authors declare no competing financial interest.

## ACKNOWLEDGMENTS

We appreciate the assistance from Ms. Su-Jen Ji (Ministry of Science and Technology of Taiwan) for SEM characterizations and from Mr. Hsueh-Ren Chen and Mr. Yu-Wen Chen (Department of Material Science and Engineering, National Taiwan University) for TEM operations. C.-C.C. was supported by a postdoctoral fellowship from National Taiwan University. Support from the Ministry of Science and Technology of Taiwan under Grant Nos. 103-2627-M-002-009, 103-2113-M-002-014-MY3 (Y.-T.C.), and 103-2113-M-032-011-MY2 (C.-C.C.) are acknowledged. Technical support from NanoCore, the Core Facilities for Nanoscience and Nanotechnology at Academia Sinica, is also acknowledged.

## REFERENCES

- (1) Li, X.; Cai, W.; An, J.; Kim, S.; Nah, J.; Yang, D.; Piner, R.; Velamakanni, A.; Jung, I.; Tutuc, E.; Banerjee, S. K.; Colombo, L.; Ruoff, R. S. Large-Area Synthesis of High-Quality and Uniform Graphene Films on Copper Foils. *Science* **2009**, *324*, 1312–1314.
- (2) Edwards, R. S.; Coleman, K. S. Graphene Film Growth on Polycrystalline Metals. *Acc. Chem. Res.* **2013**, *46*, 23–30.
- (3) Mattevi, C.; Kim, H.; Chhowalla, M. A Review of Chemical Vapour Deposition of Graphene on Copper. *J. Mater. Chem.* **2011**, *21*, 3324–3334.
- (4) Zhang, Y.; Zhang, L.; Zhou, C. Review of Chemical Vapor Deposition of Graphene and Related Applications. *Acc. Chem. Res.* **2013**, *46*, 2329–2339.
- (5) Yan, Z.; Peng, Z.; Tour, J. M. Chemical Vapor Deposition of Graphene Single Crystals. *Acc. Chem. Res.* **2014**, *47*, 1327–1337.

- (6) Wofford, J. M.; Nie, S.; McCarty, K. F.; Bartelt, N. C.; Dubon, O. D. Graphene Islands on Cu Foils: The Interplay between Shape, Orientation, and Defects. *Nano Lett.* **2010**, *10*, 4890–4896.
- (7) Yu, Q.; Jauregui, L. A.; Wu, W.; Colby, R.; Tian, J.; Su, Z.; Cao, H.; Liu, Z.; Pandey, D.; Wei, D.; Chung, T. F.; Peng, P.; Guisinger, N. P.; Stach, E. A.; Bao, J.; Pei, S.-S.; Chen, Y. P. Control and Characterization of Individual Grains and Grain Boundaries in Graphene Grown by Chemical Vapor Deposition. *Nat. Mater.* **2011**, *10*, 443–449.
- (8) Bagri, A.; Kim, S.-P.; Ruoff, R. S.; Shenoy, V. B. Thermal Transport across Twin Grain Boundaries in Polycrystalline Graphene from Nonequilibrium Molecular Dynamics Simulations. *Nano Lett.* **2011**, *11*, 3917–3921.
- (9) Grantab, R.; Shenoy, V. B.; Ruoff, R. S. Anomalous Strength Characteristics of Tilt Grain Boundaries in Graphene. *Science* **2010**, *330*, 946–948.
- (10) Haque, M. A.; Saif, M. T. A. Deformation Mechanisms in Free-Standing Nanoscale Thin Films: A Quantitative in Situ Transmission Electron Microscope Study. *Proc. Natl. Acad. Sci. U. S. A.* **2004**, *101*, 6335–6340.
- (11) Chen, S.; Brown, L.; Levendorf, M.; Cai, W.; Ju, S.-Y.; Edgeworth, J.; Li, X.; Magnuson, C. W.; Velamakanni, A.; Piner, R. D.; Kang, J.; Park, J.; Ruoff, R. S. Oxidation Resistance of Graphene-Coated Cu and Cu/Ni Alloy. *ACS Nano* **2011**, *5*, 1321–1327.
- (12) Hao, Y.; Bharathi, M. S.; Wang, L.; Liu, Y.; Chen, H.; Nie, S.; Wang, X.; Chou, H.; Tan, C.; Fallahzad, B.; Ramanarayan, H.; Magnuson, C. W.; Tutuc, E.; Yakobson, B. I.; McCarty, K. F.; Zhang, Y.-W.; Kim, P.; Hone, J.; Colombo, L.; Ruoff, R. S. The Role of Surface Oxygen in the Growth of Large Single-Crystal Graphene on Copper. *Science* **2013**, *342*, 720–723.
- (13) Li, X.; Magnuson, C. W.; Venugopal, A.; Tromp, R. M.; Hannon, J. B.; Vogel, E. M.; Colombo, L.; Ruoff, R. S. Large-Area Graphene Single Crystals Grown by Low-Pressure Chemical Vapor Deposition of Methane on Copper. *J. Am. Chem. Soc.* **2011**, *133*, 2816–2819.
- (14) Chen, S.; Ji, H.; Chou, H.; Li, Q.; Li, H.; Suk, J. W.; Piner, R.; Liao, L.; Cai, W.; Ruoff, R. S. Millimeter-Size Single-Crystal Graphene by Suppressing Evaporative Loss of Cu During Low Pressure Chemical Vapor Deposition. *Adv. Mater.* **2013**, *25*, 2062–2065.
- (15) Mohsin, A.; Liu, L.; Liu, P.; Deng, W.; Ivanov, I. N.; Li, G.; Dyck, O. E.; Duscher, G.; Dunlap, J. R.; Xiao, K.; Gu, G. Synthesis of Millimeter-Size Hexagon-Shaped Graphene Single Crystals on Resolidified Copper. *ACS Nano* **2013**, *7*, 8924–8931.
- (16) Yan, Z.; Lin, J.; Peng, Z.; Sun, Z.; Zhu, Y.; Li, L.; Xiang, C.; Samuel, E. L.; Kittrell, C.; Tour, J. M. Toward the Synthesis of Wafer-Scale Single-Crystal Graphene on Copper Foils. *ACS Nano* **2012**, *6*, 9110–9117.
- (17) Zhou, H.; Yu, W. J.; Liu, L.; Cheng, R.; Chen, Y.; Huang, X.; Liu, Y.; Wang, Y.; Huang, Y.; Duan, X. Chemical Vapor Deposition Growth of Large Single Crystals of Monolayer and Bilayer Graphene. *Nat. Commun.* **2013**, *4*, 2096.
- (18) Eres, G.; Regmi, M.; Rouleau, C. M.; Chen, J.; Ivanov, I. N.; Puzos, A. A.; Geoghegan, D. B. Cooperative Island Growth of Large-Area Single-Crystal Graphene on Copper Using Chemical Vapor Deposition. *ACS Nano* **2014**, *8*, 5657–5669.
- (19) Gan, L.; Luo, Z. Turning off Hydrogen to Realize Seeded Growth of Subcentimeter Single-Crystal Graphene Grains on Copper. *ACS Nano* **2013**, *7*, 9480–9488.
- (20) Wang, H.; Wang, G.; Bao, P.; Yang, S.; Zhu, W.; Xie, X.; Zhang, W.-J. Controllable Synthesis of Submillimeter Single-Crystal Monolayer Graphene Domains on Copper Foils by Suppressing Nucleation. *J. Am. Chem. Soc.* **2012**, *134*, 3627–3630.
- (21) Zhang, Y.; Zhang, L.; Kim, P.; Ge, M.; Li, Z.; Zhou, C. Vapor Trapping Growth of Single-Crystalline Graphene Flowers: Synthesis, Morphology, and Electronic Properties. *Nano Lett.* **2012**, *12*, 2810–2816.
- (22) Wang, C.; Chen, W.; Han, C.; Wang, G.; Tang, B.; Tang, C.; Wang, Y.; Zou, W.; Chen, W.; Zhang, X.-A.; Qin, S.; Chang, S.; Wang, L. Growth of Millimeter-Size Single Crystal Graphene on Cu Foils by Circumfluence Chemical Vapor Deposition. *Sci. Rep.* **2014**, *4*, 4537.
- (23) Jia, C.; Jiang, J.; Gan, L.; Guo, X. Direct Optical Characterization of Graphene Growth and Domains on Growth Substrates. *Sci. Rep.* **2012**, *2*, 707.
- (24) Bhaviripudi, S.; Jia, X.; Dresselhaus, M. S.; Kong, J. Role of Kinetic Factors in Chemical Vapor Deposition Synthesis of Uniform Large Area Graphene Using Copper Catalyst. *Nano Lett.* **2010**, *10*, 4128–4133.
- (25) Bansal, R. K. *A Text Book of Fluid Mechanics and Hydraulic Machines*; Laxmi Publications Limited: New Delhi, India, 2005; pp 607–632.
- (26) Artyukhov, V. I.; Liu, Y.; Yakobson, B. I. Equilibrium at the Edge and Atomistic Mechanisms of Graphene Growth. *Proc. Natl. Acad. Sci. U. S. A.* **2012**, *109*, 15136–15140.
- (27) Wu, P.; Zhang, W.; Li, Z.; Yang, J. Mechanisms of Graphene Growth on Metal Surfaces: Theoretical Perspectives. *Small* **2014**, *10*, 2136–2150.
- (28) Witten, T. A.; Sander, L. M. Diffusion-Limited Aggregation, a Kinetic Critical Phenomenon. *Phys. Rev. Lett.* **1981**, *47*, 1400–1403.
- (29) Kukovitsky, E. F.; Lvov, S. G. Increased Carbon Chemical Vapor Deposition and Carbon Nanotube Growth on Metal Substrates in Confined Spaces. *ECS J. Solid State Sci. Technol.* **2013**, *2*, M1–M8.
- (30) Probst, R. F. *Physicochemical Hydrodynamics: An Introduction*; Butterworth-Heinemann: 2013; pp 45–48.
- (31) Meca, E.; Lowengrub, J.; Kim, H.; Mattevi, C.; Shenoy, V. B. Epitaxial Graphene Growth and Shape Dynamics on Copper: Phase-Field Modeling and Experiments. *Nano Lett.* **2013**, *13*, 5692–5697.
- (32) Guo, W.; Wu, B.; Li, Y.; Wang, L.; Chen, J.; Chen, B.; Zhang, Z.; Peng, L.; Wang, S.; Liu, Y. Governing Rule for Dynamic Formation of Grain Boundaries in Grown Graphene. *ACS Nano* **2015**, *9*, 5792–5798.
- (33) Ferrari, A. C.; Meyer, J. C.; Scardaci, V.; Casiraghi, C.; Lazzeri, M.; Mauri, F.; Piscanec, S.; Jiang, D.; Novoselov, K. S.; Roth, S.; Geim, A. K. Raman Spectrum of Graphene and Graphene Layers. *Phys. Rev. Lett.* **2006**, *97*, 187401.
- (34) Malard, L. M.; Pimenta, M. A.; Dresselhaus, G.; Dresselhaus, M. S. Raman Spectroscopy in Graphene. *Phys. Rep.* **2009**, *473*, 51–87.
- (35) Ferrari, A. C.; Basko, D. M. Raman Spectroscopy as a Versatile Tool for Studying the Properties of Graphene. *Nat. Nanotechnol.* **2013**, *8*, 235–246.
- (36) Pimenta, M. A.; Dresselhaus, G.; Dresselhaus, M. S.; Cancado, L. G.; Jorio, A.; Saito, R. Studying Disorder in Graphite-Based Systems by Raman Spectroscopy. *Phys. Chem. Chem. Phys.* **2007**, *9*, 1276–1290.
- (37) Meyer, J. C.; Geim, A. K.; Katsnelson, M. I.; Novoselov, K. S.; Booth, T. J.; Roth, S. The Structure of Suspended Graphene Sheets. *Nature* **2007**, *446*, 60–63.
- (38) Hernandez, Y.; Nicolosi, V.; Lotya, M.; Blighe, F. M.; Sun, Z.; De, S.; McGovern, I. T.; Holland, B.; Byrne, M.; Gun'Ko, Y. K.; Boland, J. J.; Niraj, P.; Duesberg, G.; Krishnamurthy, S.; Goodhue, R.; Hutchison, J.; Scardaci, V.; Ferrari, A. C.; Coleman, J. N. High-Yield Production of Graphene by Liquid-Phase Exfoliation of Graphite. *Nat. Nanotechnol.* **2008**, *3*, 563–568.
- (39) Horiuchi, S.; Gotou, T.; Fujiwara, M.; Sotoaka, R.; Hirata, M.; Kimoto, K.; Asaka, T.; Yokosawa, T.; Matsui, Y.; Watanabe, K.; Sekita, M. Carbon Nanofilm with a New Structure and Property. *Jpn. J. Appl. Phys.* **2003**, *42*, L1073.
- (40) Zhang, Y.; Tan, Y.-W.; Stormer, H. L.; Kim, P. Experimental Observation of the Quantum Hall Effect and Berry's Phase in Graphene. *Nature* **2005**, *438*, 201–204.
- (41) Novoselov, K. S.; Geim, A. K.; Morozov, S. V.; Jiang, D.; Zhang, Y.; Dubonos, S. V.; Grigorieva, I. V.; Firsov, A. A. Electric Field Effect in Atomically Thin Carbon Films. *Science* **2004**, *306*, 666–669.
- (42) Tan, Y. W.; Zhang, Y.; Bolotin, K.; Zhao, Y.; Adam, S.; Hwang, E. H.; Das Sarma, S.; Stormer, H. L.; Kim, P. Measurement of Scattering Rate and Minimum Conductivity in Graphene. *Phys. Rev. Lett.* **2007**, *99*, 246803.
- (43) Dean, C. R.; Young, A. F.; Meric, I.; Lee, C.; Wang, L.; Sorgenfrei, S.; Watanabe, K.; Taniguchi, T.; Kim, P.; Shepard, K. L.;

Hone, J. Boron Nitride Substrates for High-Quality Graphene Electronics. *Nat. Nanotechnol.* **2010**, *5*, 722–726.

(44) Hwang, E. H.; Adam, S.; Das Sarma, S. Carrier Transport in Two-Dimensional Graphene Layers. *Phys. Rev. Lett.* **2007**, *98*, 186806.

(45) Chen, J.-H.; Jang, C.; Xiao, S.; Ishigami, M.; Fuhrer, M. S. Intrinsic and Extrinsic Performance Limits of Graphene Devices on SiO<sub>2</sub>. *Nat. Nanotechnol.* **2008**, *3*, 206–209.

(46) Wu, T.; Ding, G.; Shen, H.; Wang, H.; Sun, L.; Jiang, D.; Xie, X.; Jiang, M. Triggering the Continuous Growth of Graphene Toward Millimeter-Sized Grains. *Adv. Funct. Mater.* **2013**, *23*, 198–203.

(47) Gao, L.; Ren, W.; Xu, H.; Jin, L.; Wang, Z.; Ma, T.; Ma, L.-P.; Zhang, Z.; Fu, Q.; Peng, L.-M.; Bao, X.; Cheng, H.-M. Repeated Growth and Bubbling Transfer of Graphene with Millimetre-Size Single-Crystal Grains Using Platinum. *Nat. Commun.* **2012**, *3*, 699.

(48) Venugopal, A.; Chan, J.; Li, X.; Magnuson, C. W.; Kirk, W. P.; Colombo, L.; Ruoff, R. S.; Vogel, E. M. Effective Mobility of Single-Layer Graphene Transistors as a Function of Channel Dimensions. *J. Appl. Phys.* **2011**, *109*, 104511.

(49) Chen, Z.; Appenzeller, J. Mobility Extraction and Quantum Capacitance Impact in High Performance Graphene Field-Effect Transistor Devices. *IEEE IEDM Tech. Digest* **2008**, *21.1*, 509–512.

(50) Meric, I.; Dean, C. R.; Young, A. F.; Baklitskaya, N.; Tremblay, N. J.; Nuckolls, C.; Kim, P.; Shepard, K. L. Channel Length Scaling in Graphene Field-Effect Transistors Studied with Pulsed Current–Voltage Measurements. *Nano Lett.* **2011**, *11*, 1093–1097.

(51) Jo, G.; Choe, M.; Lee, S.; Park, W.; Kahng, Y. H.; Lee, T. The Application of Graphene as Electrodes in Electrical and Optical Devices. *Nanotechnology* **2012**, *23*, 112001.

(52) Benjamin, D. Thermal Transport and Photo-Induced Charge Transport in Graphene. Ph.D. Thesis, Georgia Institute of Technology, Atlanta, GA, 2011.

(53) Zhang, Y.; Li, Z.; Kim, P.; Zhang, L.; Zhou, C. Anisotropic Hydrogen Etching of Chemical Vapor Deposited Graphene. *ACS Nano* **2012**, *6*, 126–132.

(54) Kim, H.; Mattevi, C.; Calvo, M. R.; Oberg, J. C.; Artiglia, L.; Agnoli, S.; Hirjibehedin, C. F.; Chhowalla, M.; Saiz, E. Activation Energy Paths for Graphene Nucleation and Growth on Cu. *ACS Nano* **2012**, *6*, 3614–3623.

# Supporting Information

## Growth of Large-Area Graphene Single Crystals in Confined Reaction Space with Diffusion-Driven Chemical Vapor Deposition

*Chiao-Chen Chen,<sup>\*,†,‡</sup> Chia-Jung Kuo,<sup>†</sup> Chun-Da Liao,<sup>†</sup> Chin-Fu Chang,<sup>†</sup> Chi-Ang Tseng,<sup>†</sup> Chia-Rung Liu<sup>†</sup> and Yit-Tsong Chen<sup>\*,†,§</sup>*

<sup>†</sup>Department of Chemistry, National Taiwan University  
No. 1, Sec. 4, Roosevelt Road  
Taipei 106, Taiwan  
E-mail: ytcchem@ntu.edu.tw

<sup>‡</sup>Department of Chemistry  
Tamkang University  
No. 151, Yingzhuan Road  
New Taipei City 25137, Taiwan  
E-mail: chence@mail.tku.edu.tw

<sup>§</sup>Institute of Atomic and Molecular Sciences  
Academia Sinica  
P.O. Box 23-166  
Taipei 106, Taiwan

## **MATERIALS AND METHODS**

### **1. Catalytic growth of graphene**

Graphene single crystals were synthesized on a 25- $\mu\text{m}$ -thick Cu foil (Alfa Aesar, purity 99.8%) in an LPCVD chamber. The reaction chamber is composed of a 90-cm-long quartz tube with 2.54 cm in outer diameter and a split-tube furnace (Thermo Scientific, Lindberg/Blue M) with a 10-cm-long heating zone (Figure S1 and 1). For graphene synthesis, the as-received Cu foil was treated with glacial acetic acid (Sigma-Aldrich,  $\geq 99.85\%$ ) for 8 hr to remove oxides and contaminations on the Cu surface, followed by thoroughly rinsing with DI water and blow-drying with  $\text{N}_2$ . The acid-treated Cu foil was then cut into  $1 \times 2 \text{ cm}^2$  strips and mounted on a tungsten (W) boat to be located in the LPCVD chamber. The tungsten boat was shifted out of the heating zone quickly via a small magnetic dragger after reaction. In the synthetic reaction, the CVD system was first evacuated to  $\sim 2 \times 10^{-2}$  torr for 10 min, followed by filling the gas mixture of Ar (FMI Corp., 99.9995%) and  $\text{H}_2$  (FMI Corp., 99.9995%). The chamber temperature was then ramped up to  $1050 \text{ }^\circ\text{C}$  within 40 min and kept at  $1050 \text{ }^\circ\text{C}$  (typically for 30 min) for the substrate annealing (Figure S2, Steps I and II). After the annealing, the system temperature was maintained at  $1050 \text{ }^\circ\text{C}$ , followed by introducing  $\text{CH}_4$  (FMI Corp., 99.9995%) as the carbon source into the reaction chamber to initiate graphene growth (Figure S2, Step III). After the reaction, while both  $\text{H}_2$  and  $\text{CH}_4$  flows were turned off, the tungsten boat containing the Cu substrate grown with graphene was quickly shifted out of the hot zone. Finally, the system was cooled to room temperature under an Ar flow (Figure S2, Step IV).

### **2. Selected oxidation-assisted optical image**

To rapidly identify how different synthesis protocols vary the graphene domains produced, we adopted the selective oxidation method, reported by C. Jia and coworkers, which enables the direct optical inspection of the as-grown graphene without going through the laborious transfer process.<sup>S1</sup> With this method, a Cu substrate with the as-grown graphene grains was oxidized in ambient air on a hot plate at  $180 \text{ }^\circ\text{C}$  for 20 min. The graphene film on the Cu substrate could serve as a protection

layer to prevent the underlying Cu surface from oxidation because of its high chemical/thermal stability and impermeability to gases and liquids.<sup>S2, 3</sup> In contrast, the surrounding surface of the Cu foil without being covered by graphene exhibited high reactivity and was readily oxidized to copper oxides with an obvious color change. The apparent color contrast between the oxidized and non-oxidized Cu surfaces made the synthesized graphene domains easy to be observed in an optical microscope (Olympus, BX51) equipped with a charge-coupled device (CCD) camera (Leica, DFC495).

### 3. Thin-film transfer

For further optical/electrical characterization and device fabrication, the as-grown graphene domains/films on the Cu substrate were transferred onto a p-doped Si wafer with a 300-nm-thick SiO<sub>2</sub> layer or a TEM grid (Electron Microscopy Sciences, LC200-Cu) via a conventional polymer-assisted method.<sup>S4</sup> Because graphene domains/films were grown on both sides of the Cu substrate, we selected one side of the Cu foil ( $1 \times 1 \text{ cm}^2$ ) to transfer the as-grown graphene by spin-coating 50  $\mu\text{L}$  of polymethyl methacrylate (MicroChem, 950 PMMA, A4) at 3000 rpm for 30 sec, followed by baking the PMMA/graphene/Cu on a hot plate at 135 °C for 5 min. Meanwhile, the other side of the Cu foil without the PMMA coating was cleaned with O<sub>2</sub> plasma to remove graphene. The plasma cleaned PMMA/graphene/Cu sample was then floated over Marble's solution (CuSO<sub>4</sub> : HCl : H<sub>2</sub>O = 10 g : 50 mL : 50 mL) to etch away the Cu substrate, resulting in a PMMA/graphene membrane suspending on the solution surface. The PMMA/graphene membrane was then transferred to DI water to further remove the remaining etchants and subsequently scooped up with a receiving substrate (a SiO<sub>2</sub>/Si wafer or a TEM grid). The PMMA/graphene membrane on the receiving substrate was vacuum dried in a desiccator at room temperature for 2 hr and heated on a hot plate at 85 °C for 15 min to promote the adhesion between graphene and the receiving substrate. The PMMA/graphene/substrate stack was then immersed into acetone at room temperature overnight to remove PMMA, followed by rinsing the graphene/substrate with isopropanol and DI water to

remove organic residues on the graphene surface. Finally, the graphene/substrate was blow-dried with N<sub>2</sub>.

#### 4. Device fabrication and electrical measurement

To fabricate field-effect-transistor (FET) devices, the graphene/substrate was first annealed at 200 °C under diluted H<sub>2</sub> flow (H<sub>2</sub> 10 sccm/Ar 100 sccm) for 1 hr to remove the remained organic residues during the transfer process. After annealing, selected domains of the graphene/substrate were mounted carefully with a TEM copper grid which served as a shadow mask for the thermal-evaporation deposition of source/drain electrodes (10 nm Cr/50 nm Au). The electrical measurements of the as-fabricated graphene-FET devices were conducted in a probe station (Lakeshore, TTPX) equipped with a source meter (Keithley, 2636A) under the chamber pressure of  $\sim 2 \times 10^{-3}$  torr at room temperature. In the measurements, a back gate voltage ( $V_g$ ) was applied through the p-doped Si substrate with a 300-nm-thick SiO<sub>2</sub> dielectric layer. From the recorded source-drain current vs. source-drain voltage ( $I_{sd}$ - $V_{sd}$ ) and source-drain current vs. gate voltage ( $I_{sd}$ - $V_g$ ) curves, the device resistance ( $R_{tot}$ ), which is composed of the contact resistance ( $R_{contact}$ ) of metal/graphene and the graphene channel resistance ( $R_{channel}$ ), can be determined.<sup>S5, 6</sup>

$$R_{tot} = \frac{V_{sd}}{I_{sd}} = R_{contact} + R_{channel} = R_{contact} + \frac{L}{W} \cdot \rho \quad (S1)$$

In Equation S1,  $L$  refers to the channel length between the source and drain electrodes,  $W$  is the channel width, and  $\rho$  denotes the channel resistivity of the graphene-FET device. In addition, the conductivity ( $\sigma = 1/\rho$ ) of the graphene channel is related to field-effect mobility ( $\mu_{EF}$ ), elementary charge ( $e$ ), and carrier density ( $n$ ) as shown in Equation S2.<sup>S6</sup>

$$\rho = \sigma^{-1} = (ne\mu_{EF})^{-1} = \left( \mu_{EF} \sqrt{e^2 n_0^2 + [C_g(V_g - V_{Dirac})]^2} \right)^{-1} \quad (S2)$$

In Equation S2,  $n_0$  is the residual carrier density at the Dirac point due to charged impurity,  $C_g$  is the capacitance per unit area of the gate dielectric, and  $V_{Dirac}$  refers to the recorded potential shift at the Dirac point. The combination of Equation S1 and S2 yields Equation S3, in which  $R_{tot}$  is

represented as a function of  $V_g - V_{Dirac}$ . It is noted that  $R_{contact}$  can be determined from Equation S3 by fitting the recorded data of  $R_{tot}$  and  $V_g - V_{Dirac}$ .<sup>S7</sup>

$$\begin{aligned}
 R_{tot} &= \frac{V_{sd}}{I_{sd}} = R_{contact} + \frac{L}{W} \cdot \rho \\
 &= R_{contact} + \frac{L}{W} \cdot \frac{1}{\mu_{EF} \sqrt{e^2 n_0^2 + [C_g (V_g - V_{Dirac})]^2}} \\
 &= R_{contact} + \frac{L}{W} \cdot \frac{1}{n_0 e \mu_{EF}} \left[ 1 + \frac{C_g^2}{n_0^2 e^2} (V_g - V_{Dirac})^2 \right]^{-1/2} \quad (S3)
 \end{aligned}$$

## 5. FEM simulation of the flow field in confined reaction space

Two COMSOL Multiphysics modules in the finite element model (FEM), i.e., laminar flow (Navier-Stokes equation) and transport of dilute species (convection-diffusion equation), were coupled to solve the flow field and mass transport of the reactants flow involved in our CVD reaction. Simulations were performed with a commercial FEM package of COMSOL Multiphysics (version 4.4). The three-dimensional geometry shown in Figure S1a describes the CVD reaction system used in this study for graphene synthesis. This system consists of a quartz tube (2.54 cm/2.15 cm in outer/inner diameter and 90 cm in length) with a rectangular reactor (L 25 mm × W 18 mm × H 4 mm) located in the center. Within the rectangular reactor, a confined reaction room (L 22 mm × W 13 mm × H 50 μm) with one open end (as an inlet) was designed to allow the insertion of a 25-μm-thick Cu foil and the entry of reacting gases. It is noteworthy that the inlet was oriented towards tailwind to prevent the direct injection of gas flow. To save the memory space required in computation and to facilitate the illustration of simulated results, a reduced three-dimensional geometry with a plane of symmetry (Figure S1b) was utilized for the FEM simulations. In addition, the graphene synthesis was conducted in the heating zone located within the central 10-cm-long region of the quartz tube (Figure 1 and S1). Therefore, our discussion about the simulated flow fields and mass transports is focused on this region (Figure S1c). In this simulation, the flow was

considered as a gas mixture of CH<sub>4</sub>, H<sub>2</sub>, and Ar with a constant inlet speed consistent with the experimental conditions. In addition, to demonstrate the scalability of the CVD method adopted in this study, a simulation for the CVD reaction system composed of a large tube furnace (Figure S6a–c, 20.32 cm in diameter and 120 cm in length, adapted from the chamber dimensions reported by Bae, S. et. al., *Nat. Nanotechnol.*, **2010**, 5, 574-578)<sup>S8</sup> with an amplified rectangular reactor (Figure S6d, L 20 cm × W 14.4 cm × H 4 mm containing a confined reaction room of L 17.6 cm × W 10.4 cm × H 50 μm) was performed.

## 6. Estimation of boundary layer thickness

Over a flat plane, the boundary layer thickness ( $\delta$ ) can be estimated with the following equation:<sup>S9, 10</sup>

$$\delta = 4.91 \sqrt{\frac{\nu x}{U}} \quad (\text{S4})$$

where  $\nu$  refers to the kinematic viscosity (m<sup>2</sup>/s),  $x$  is the distance downstream from the start of the boundary layer (m) and  $U$  is the free stream velocity (m/s). In the LPCVD system at 1050 °C and 1.71 torr, the kinematic viscosity of  $\nu \sim 1 \times 10^{-2}$  m<sup>2</sup>/s was estimated for the reactant mixture (i.e., H<sub>2</sub>, CH<sub>4</sub>, and Ar).<sup>S11</sup> The free stream velocity ( $U$ ) at the entrance of the confined reaction space is  $\sim 1 \times 10^{-2}$  m/s obtained from the FEM simulation. Since the Cu substrate was located typically at  $\sim 1$  mm away from the entrance of the confined reaction space, the distance from the start of the boundary ( $x$ ) was assumed to be  $10^{-3}$  m in the calculation. From the calculation with Equation S4,

$$\delta = 4.91 \sqrt{\frac{\nu x}{U}} = 4.91 \sqrt{\frac{10^{-2} \times 10^{-3}}{10^{-2}}} = 0.16 \text{ m} = 16 \text{ cm}.$$

Since the height of the confined reaction room to accommodate the catalytic Cu substrate is only 50 μm, the boundary layer is believed to extend over the entire space between the Cu surface and quartz slides.

**Table S1.** Synthesis protocols utilized in this study

| Protocol   | Temp<br>(°C) | Annealing step     |              |                          |               | Growing step       |              |                          |                           |               | Reactor type                           | Grain size<br>( $\mu\text{m}$ ) | Grain density<br>(nuclei/ $\text{cm}^2$ ) |
|------------|--------------|--------------------|--------------|--------------------------|---------------|--------------------|--------------|--------------------------|---------------------------|---------------|--|---------------------------------|---|
|            |              | Pressure<br>(torr) | Ar<br>(sccm) | H <sub>2</sub><br>(sccm) | Time<br>(min) | Pressure<br>(torr) | Ar<br>(sccm) | H <sub>2</sub><br>(sccm) | CH <sub>4</sub><br>(sccm) | Time<br>(min) |  |                                 |   |
| <b>P1</b>  | 1050         | 1.04               | 200          | 50                       | 60            | 0.18               | 0            | 25                       | 1                         | 20            | on W boat                              | ~15                             | ~9.6E+5                                   |
| <b>P2</b>  | 1050         | 1.04               | 200          | 50                       | 60            | 0.18               | 0            | 25                       | 1                         | 90            | sandwiched<br>between<br>quartz slides | ~50                             | ~6.8E+4                                   |
| <b>P3</b>  | 1050         | 1.04               | 200          | 50                       | 60            | 3.43               | 1000         | 25                       | 1                         | 25            | Confined<br>space                      | ~20                             | ~4.7E+4                                   |
| <b>P4</b>  | 1050         | 1.03               | 200          | 10                       | 60            | 1.71               | 500          | 22                       | 1                         | 60            |  | ~100                            | ~1.2E+4                                   |
| <b>P5</b>  | 1050         | 1.67               | 500          | 10                       | 60            | 1.71               | 500          | 22                       | 1                         | 100           |  | ~150                            | ~8.7E+3                                   |
| <b>P6</b>  | 1050         | 2.45               | 1000         | 10                       | 60            | 1.71               | 500          | 22                       | 1                         | 105           |  | ~200                            | ~5.7E+3                                   |
| <b>P7</b>  | 1050         | 3.12               | 1500         | 10                       | 60            | 1.71               | 500          | 22                       | 1                         | 135           |  | ~250                            | ~4.4E+3                                   |
| <b>P8</b>  | 1050         | 3.69               | 2000         | 10                       | 60            | 1.71               | 500          | 22                       | 1                         | 155           | Confined<br>space                      | ~300                            | ~2.8E+3                                   |
| <b>P9</b>  | 1050         | 3.12               | 1500         | 10                       | 30            | 1.71               | 500          | 22                       | 1                         | 165           |  | ~300                            | ~4.0E+3                                   |
| <b>P10</b> | 1050         | 3.69               | 2000         | 10                       | 30            | 1.71               | 500          | 22                       | 1                         | 180           |  | ~350                            | ~2.5E+3                                   |
| <b>P11</b> | 1050         | 3.67               | 2000         | 8                        | 30            | 1.71               | 500          | 22                       | 1                         | 240           |  | ~550                            | ~6.3E+2                                   |
| <b>P12</b> | 1050         | 3.65               | 2000         | 5                        | 30            | 1.71               | 500          | 22                       | 1                         | 270           |  | ~800                            | ~2.1E+2                                   |
| <b>P13</b> | 1050         | 3.69               | 1500         | 10                       | 60            | 1.30               | 330          | 28                       | 1                         | 120           |  | ~180*                           | ~8.2E+2*                                  |

\*These results are obtained using the reactor with a gap size of 50  $\mu\text{m}$ .

**Table S2.** Performance parameters of representative protocols for the synthesis of large graphene single crystals.

| Ref.      | Maximum Grain size (mm) | Averaged growth rate ( $\mu\text{m}/\text{min}$ ) | Duration of a synthesis cycle to obtain 0.8 mm graphene grain* (min) | Electrical mobility ( $\text{cm}^2\text{V}^{-1}\text{s}^{-1}$ ) | Required highest temperature ( $^{\circ}\text{C}$ ) |
|-----------|-------------------------|---|--|---|---|
| 12        | 10                      | 13.9  | 90   | 15000~30000   | 1035  |
| 13        | 0.5 <sup>†</sup>        | 6   | N. A.  | 4000  | 1035  |
| 14        | 2                       | 5.6   | 160  | 5200  | 1035  |
| 15        | 1.1                     | 3.6   | 340  | N. A.   | 1100  |
| 16        | 2.3                     | 18.4  | 460  | 11000   | 1077  |
| 17        | 5                       | 2.1   | 400  | 16000   | 1070  |
| 20        | 0.61                    | 22  | N. A.  | N. A.   | 1045  |
| 21        | 0.1                     | 3.3   | N. A.  | 4200  | 1000  |
| 22        | 1.2                     | 4   | 320  | 2440  | 1050  |
| This work | 0.84                    | 3.1   | 300  | 4800  | 1050  |

\*Duration of a synthesis cycle includes the annealing and growth periods to obtain a graphene grain with 0.8 mm in diameter.

<sup>†</sup>Performance parameters that are less superior or comparable to this work are marked with shading for easier comparison.

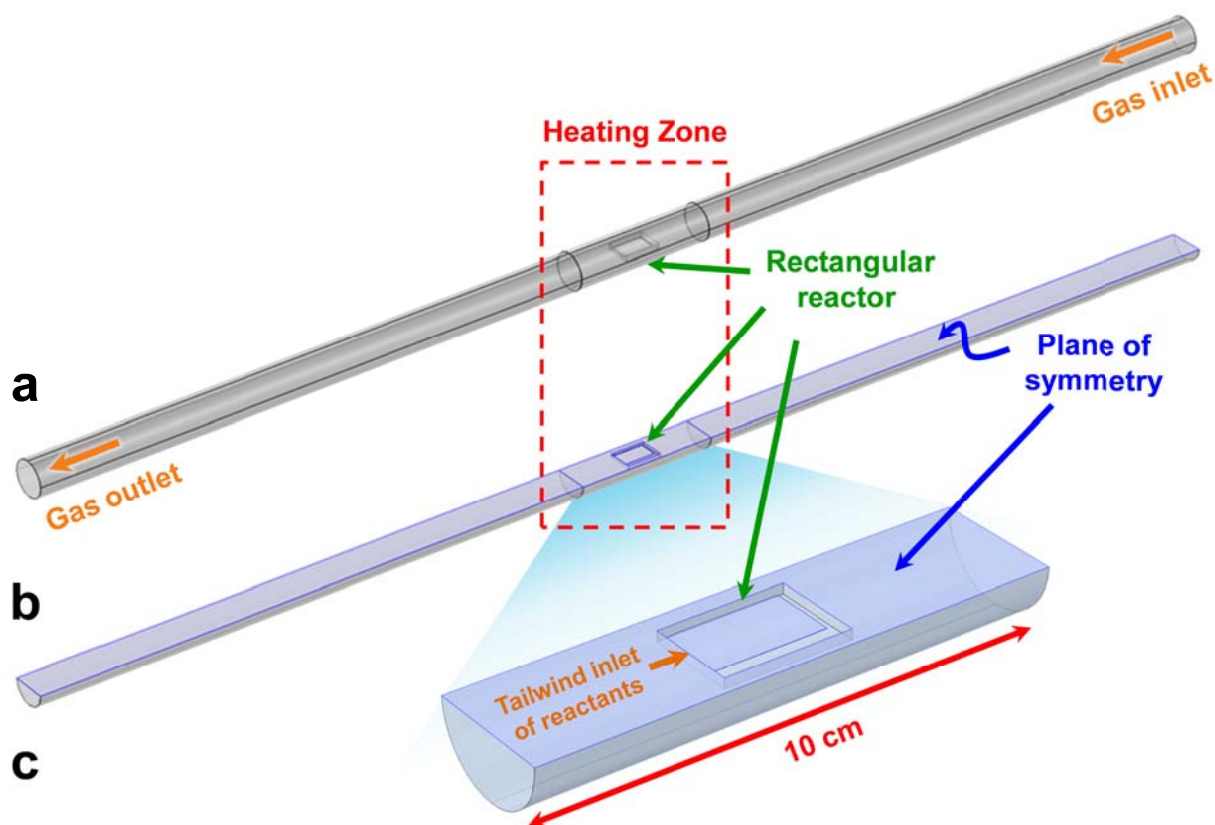


**Figure S1.** (a) The three-dimensional geometry of the CVD system utilized in this study. This system consists of a quartz tube (2.54 cm/2.15 cm in outer/inner diameter and 90 cm in length) and a rectangular reactor (L 25 mm  $\times$  W 18 mm  $\times$  H 4 mm) located in the central 10-cm-long heating zone. A confined reaction space (L 22 mm  $\times$  W 13 mm  $\times$  H 50  $\mu$ m) with one open end (as an inlet) was designed to allow the insertion of a 25- $\mu$ m-thick Cu foil and the entry of reacting gases. The inlet of reacting gases was oriented towards tailwind to prevent the direct injection of gas flow. (b) The reduced three-dimensional geometry of (a) with a plane of symmetry utilized in the FEM simulations. (c) An enlarged diagram of (b) with an emphasis on the 10-cm-long heating zone.

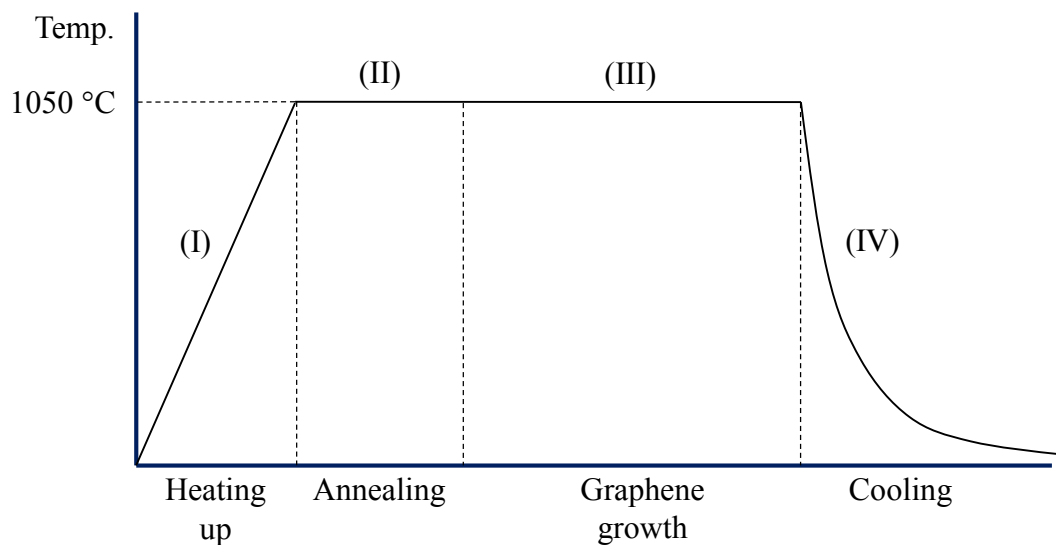


**Figure S2.** A workflow diagram for the graphene synthesis in LPCVD reaction employed in this study. Experimental details for the chamber pressure, flow rate of each reacting gas, and elapsed reaction time involved in the annealing and growing stages are tabulated in Table S1. In all tests, the ramp-up time for the chamber temperature, from 25 to 1050 °C, at the heating-up stage was 40 min.

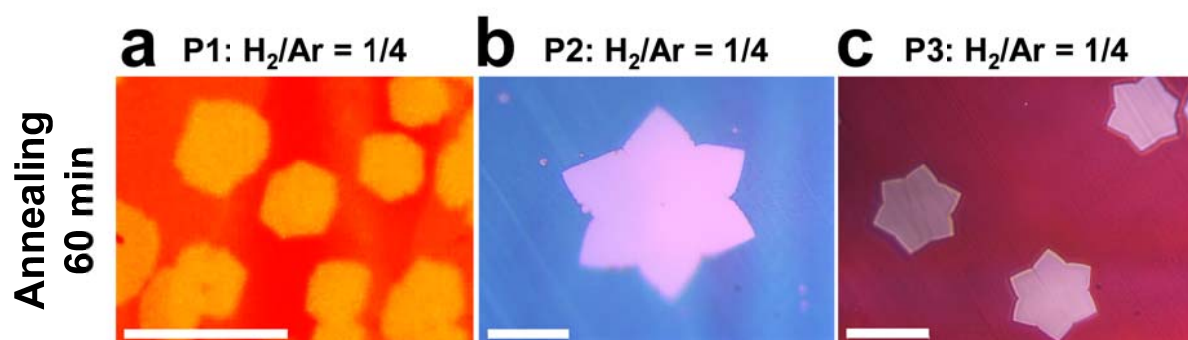


**Figure S3.** Enlarged optical micrographs of the as-synthesized graphene grains shown in Figure 2d–f for easier comparison of the graphene-shape transformation due to different growth-controlling mechanisms, i.e., surface-reaction (edge-attachment) versus mass-transport (diffusion).

Scale bars: 20  $\mu\text{m}$ .

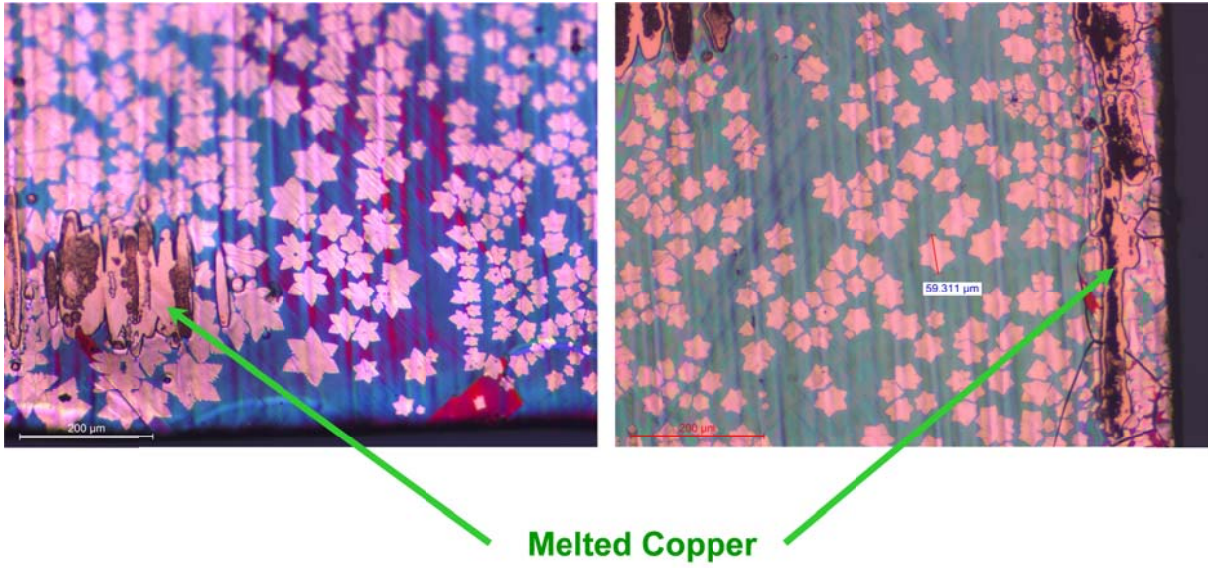


**Figure S4.** Parts of the Cu substrate melted at elevated temperature to coalesce with the reactor, making it difficult to remove the as-grown graphene/Cu substrate from quartz slides after the reaction for further optical characterization and device fabrication.

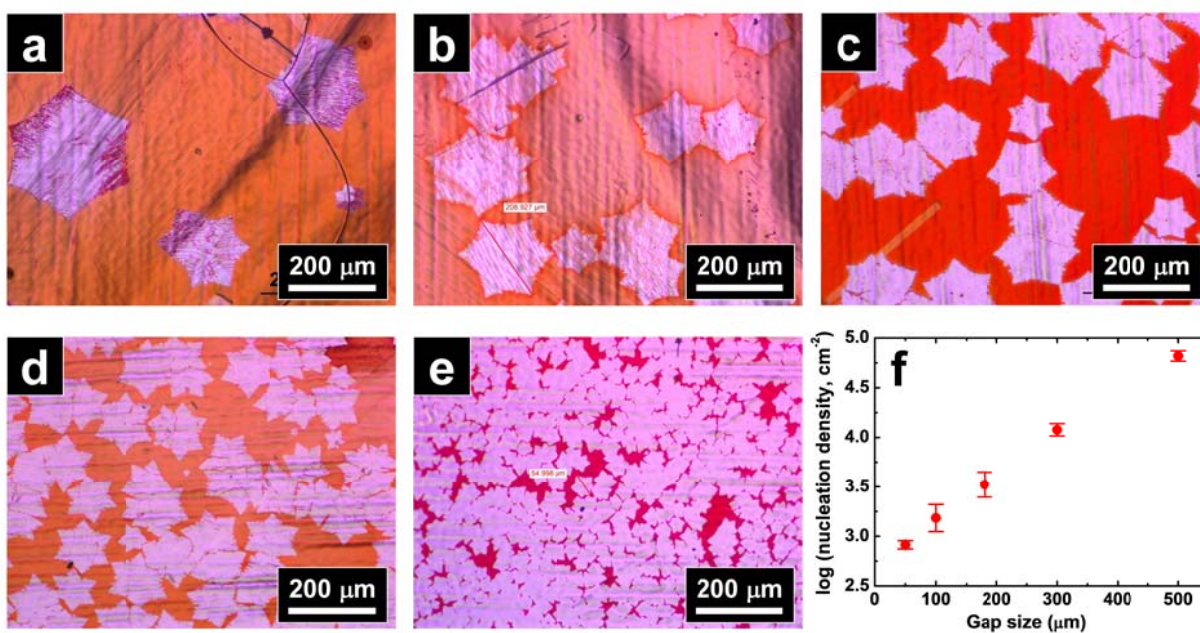


**Figure S5.** With the same synthesis protocol (Table S1, P13), graphene samples obtained from five reactors of different gap sizes, (a) 50  $\mu\text{m}$ , (b) 100  $\mu\text{m}$ , (c) 180  $\mu\text{m}$ , (d) 300  $\mu\text{m}$ , and (e) 500  $\mu\text{m}$ , were investigated to find the optimal gap size for a 25- $\mu\text{m}$ -thick Cu catalytic foil. (f) The resultant nucleation density decreases monotonically with the reduction of gap size.

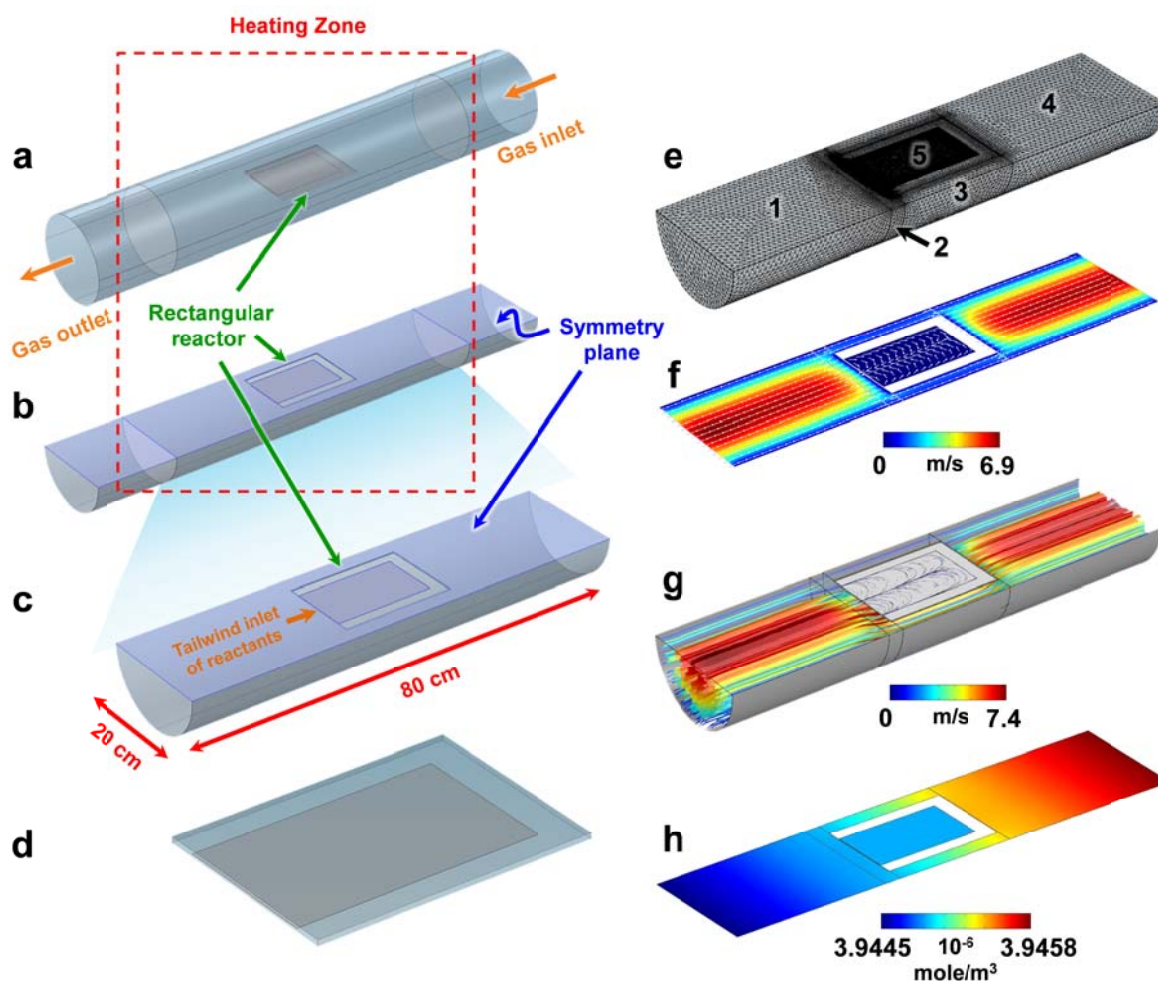


**Figure S6.** (a–b) The three-dimensional geometry of an enlarged CVD system composed of a quartz tube (20.32 cm in outer diameter and 120 cm in length) with a rectangular reactor (L 20 cm  $\times$  W 14.4 cm  $\times$  H 4 mm) located in the central heating zone of 80 cm in length. (c) The reduced three-dimensional geometry of (a) with a plane of symmetry utilized in the FEM simulation. The inlet of reacting gases was also oriented towards tailwind to prevent the direct injection of gas flow. (d) The zoom-in geometry of the rectangular reactor with a confined reaction space of L 17.6 cm  $\times$  W 10.4 cm  $\times$  H 50  $\mu\text{m}$ . (e) The meshed geometry of (c) illustrates that different domains were meshed with different space resolutions to achieve the most efficient simulation. The simulation results of this enlarged CVD system show that the fluid conditions, including (f) reduced flow velocity, (g) diffusion-dominant fluxes, and (h) a homogenous reactant distribution, are similar to those (shown in Figure 1) of the chamber/reactor with much smaller dimensions.

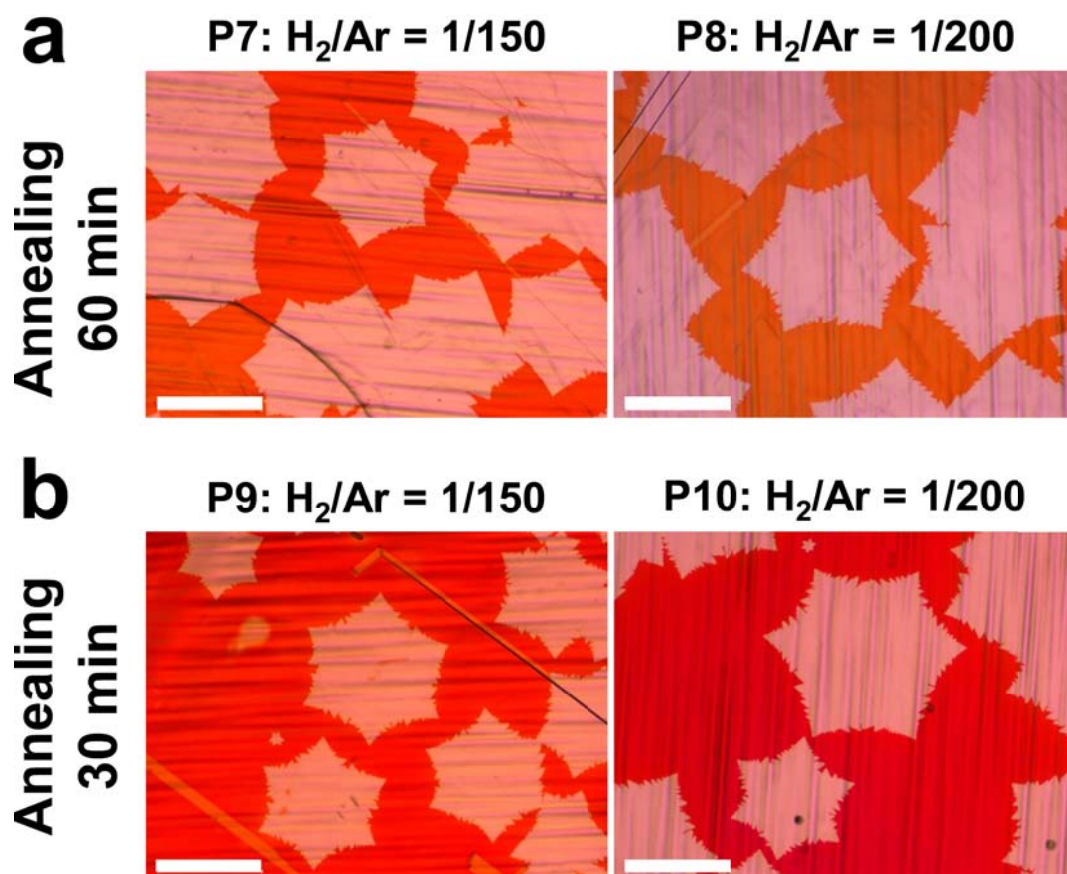


**Figure S7.** Comparison of the as-grown graphene grains from the same synthesis protocols except the  $H_2$  exposure time during annealing. These results demonstrate that, apart from the reduction of  $H_2$  concentration, the shortened exposure time to  $H_2$  during annealing further lessens the nucleation density. Scale bars: 200  $\mu m$ .

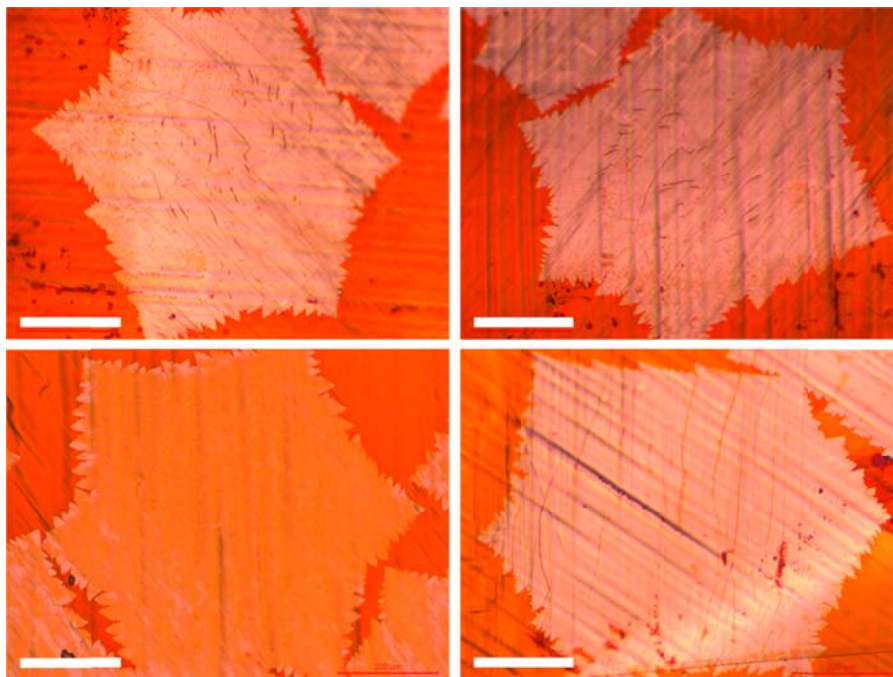


**Figure S8.** Representative examples of the large-area graphene single crystals synthesized from different experimental batches with the optimized synthesis protocol of P12. Scale bars: 200  $\mu\text{m}$ .

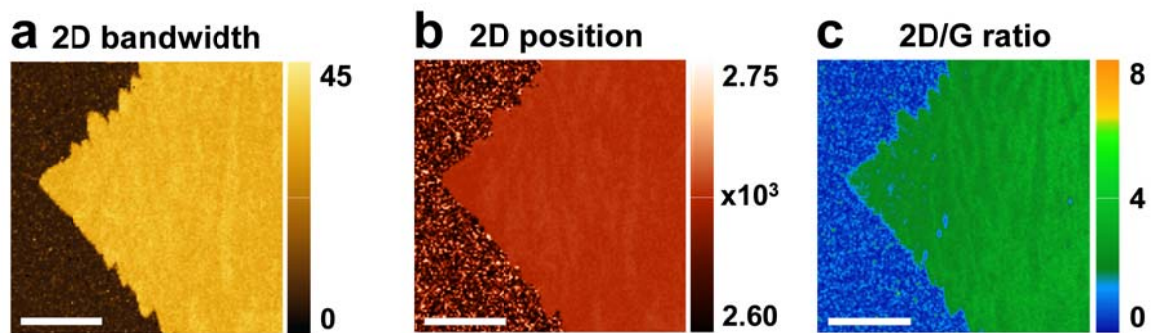


**Figure S9.** Raman mappings of the 2D bandwidth (FWHM), 2D peak position, and intensity ratio of  $I_{2D}/I_G$  collected from the selected area marked by a red-dashed square in Figure 4a. Scale bars: 30  $\mu\text{m}$ .

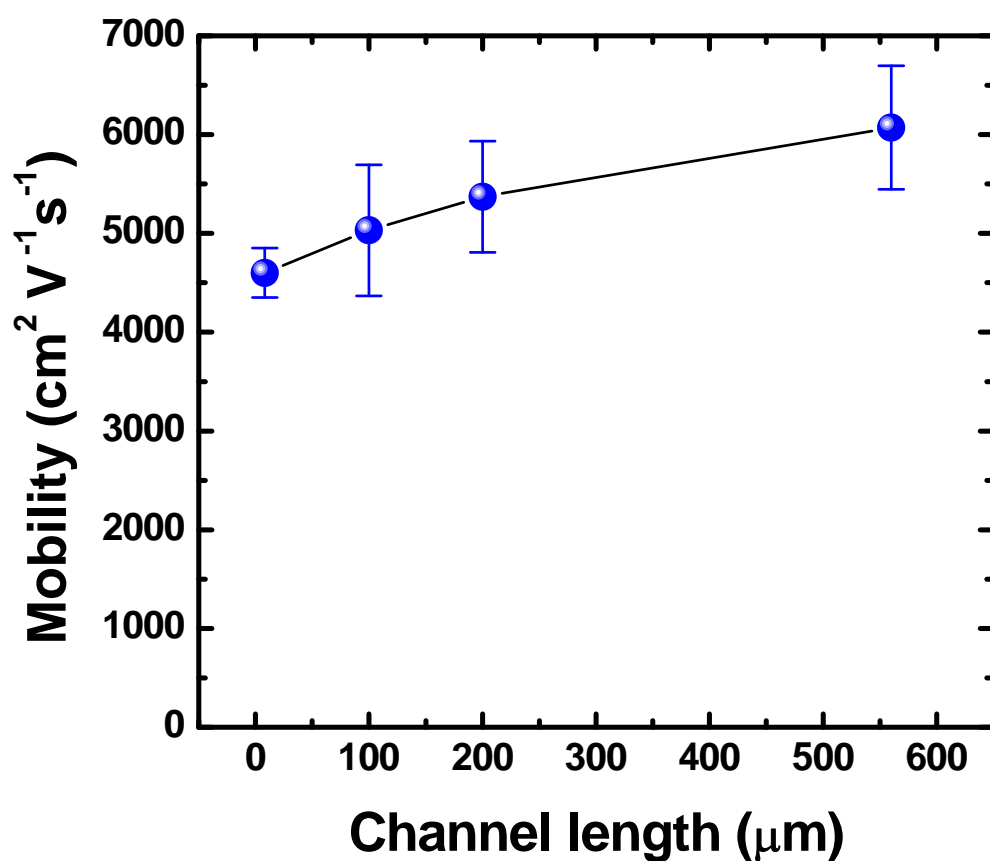


**Figure S10.** The electrical measurements show that the field-effect mobility of graphene devices is dependent on the channel length ( $L_{\text{ch}}$ ) ranging from 8, 100, 200, to 560  $\mu\text{m}$ , where the channel width ( $W_{\text{ch}}$ ) of the graphene devices was maintained to be  $>50 \mu\text{m}$  to minimize the effect of width-dependent mobility.

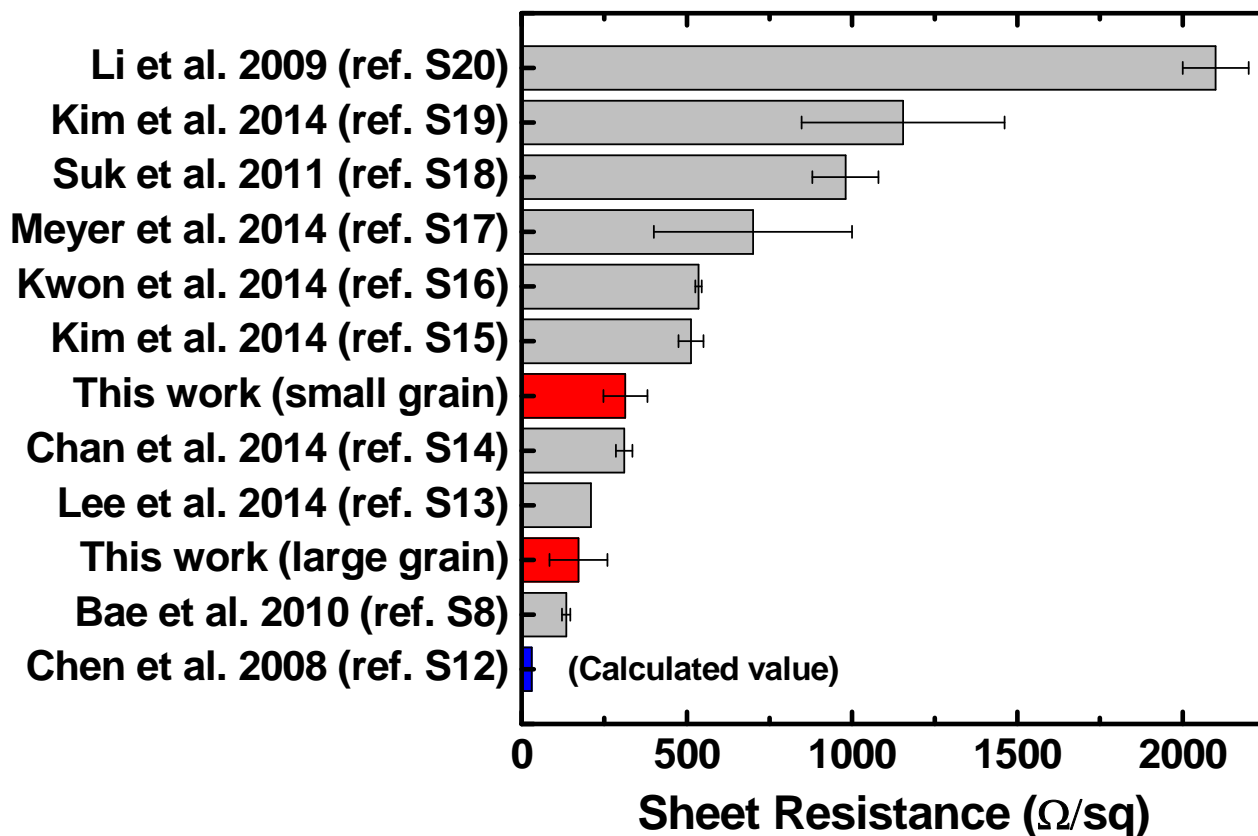


**Figure S11.** Comparison of the sheet resistances of several pristine CVD-synthesized monolayer graphene films. While the intrinsic sheet resistance of graphene is estimated to be  $\sim 30 \text{ } \Omega/\text{sq}$  as indicated with a blue bar,<sup>S12</sup> the sheet resistances reported recently by several representative groups are illustrated with gray bars.<sup>S8, 13-20</sup> For the continuous graphene films prepared in this study (marked by red), the sheet resistances are determined to be  $171.9 \pm 87.4 \text{ } \Omega/\text{sq}$  for the graphene films composed of multiple large graphene single crystals and  $367.7 \pm 120.5 \text{ } \Omega/\text{sq}$  for those films that consist of multiple small graphene grains.

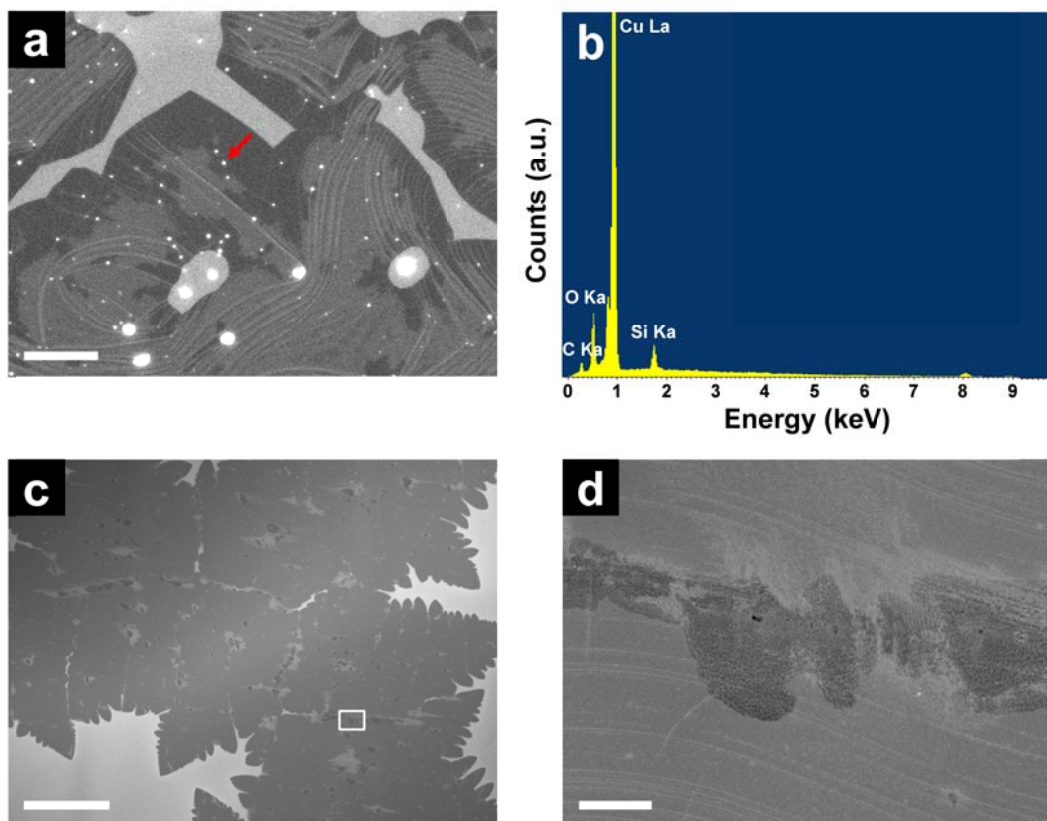


**Figure S12.** (a) An SEM image shows the significant contamination of SiO<sub>2</sub> nanoparticles (small white dots) on the as-grown graphene on a Cu substrate, which was obtained from a conventional CVD reaction (Figure 2a). (b) The nanoparticle, marked with a red arrow in (a), was analyzed by energy-dispersive X-ray spectroscopy (EDS) to comprise silicon and oxygen, resulting from the H<sub>2</sub> etching of a quartz tube in the graphene synthesis. (c) In sharp contrast, the as-grown graphene synthesized within a confined reaction room (Figure 2c) is free of SiO<sub>2</sub> contamination. (d) A zoom-in image of the area marked with a white square in (c) further confirms the cleanness of the graphene surface. Scale bars: (a) 2 μm, (c) 40 μm, and (d) 2 μm.

## Reference

- S1. Jia, C.; Jiang, J.; Gan, L.; Guo, X. Direct Optical Characterization of Graphene Growth and Domains on Growth Substrates. *Sci. Rep.*, **2012**, *2*, 707.
- S2. Bunch, J. S.; Verbridge, S. S.; Alden, J. S.; van der Zande, A. M.; Parpia, J. M.; Craighead, H. G.; McEuen, P. L. Impermeable Atomic Membranes from Graphene Sheets. *Nano Lett.*, **2008**, *8*, 2458-2462.
- S3. Su, Y.; Kravets, V. G.; Wong, S. L.; Waters, J.; Geim, A. K.; Nair, R. R. Impermeable Barrier Films and Protective Coatings Based on Reduced Graphene Oxide. *Nat. Commun.*, **2014**, *5*, 4843.
- S4. Kang, J.; Shin, D.; Bae, S.; Hong, B. H. Graphene Transfer: Key for Applications. *Nanoscale*, **2012**, *4*, 5527-5537.
- S5. Kim, S.; Nah, J.; Jo, I.; Shahrjerdi, D.; Colombo, L.; Yao, Z.; Tutuc, E.; Banerjee, S. K. Realization of a High Mobility Dual-Gated Graphene Field-Effect Transistor with Al<sub>2</sub>O<sub>3</sub> Dielectric. *Appl. Phys. Lett.*, **2009**, *94*, 062107.
- S6. Liao, L.; Bai, J.; Qu, Y.; Lin, Y.-c.; Li, Y.; Huang, Y.; Duan, X. High- $\kappa$  Oxide Nanoribbons as Gate Dielectrics for High Mobility Top-Gated Graphene Transistors. *Proc. Natl. Acad. Sci. USA*, **2010**, *107*, 6711-6715.
- S7. Liu, L.; Zhou, H.; Cheng, R.; Yu, W. J.; Liu, Y.; Chen, Y.; Shaw, J.; Zhong, X.; Huang, Y.; Duan, X. High-Yield Chemical Vapor Deposition Growth of High-Quality Large-Area AB-Stacked Bilayer Graphene. *ACS Nano*, **2012**, *6*, 8241-8249.
- S8. Bae, S.; Kim, H.; Lee, Y.; Xu, X.; Park, J.-S.; Zheng, Y.; Balakrishnan, J.; Lei, T.; Ri Kim, H.; Song, Y. I.; Kim, Y.-J.; Kim, K. S.; Ozyilmaz, B.; Ahn, J.-H.; Hong, B. H.; Iijima, S. Roll-to-Roll Production of 30-inch Graphene Films for Transparent Electrodes. *Nat. Nanotechnol.*, **2010**, *5*, 574-578.
- S9. Blasius, H. Grenzschichten in Flüssigkeiten mit kleiner Reibung. *Z. Math. Phys.*, **1908**, *56*, 1-37.

- S10. Rubin, H., *Environmental Fluid Mechanics*, CRC Press: Florida, USA, 2001; pp 251-258.
- S11. Wallard, A.; Sené, M.; Craston, D.; Williams, J.; Milton, M., *Tables of Physical & Chemical Constants*, Kaye & Laby Online, [http://www.kayelaby.npl.co.uk/general\\_physics/2\\_2/2\\_2\\_3.html](http://www.kayelaby.npl.co.uk/general_physics/2_2/2_2_3.html), Accessed March 15, 2015.
- S12. Chen, J.-H.; Jang, C.; Xiao, S.; Ishigami, M.; Fuhrer, M. S. Intrinsic and Extrinsic Performance Limits of Graphene Devices on SiO<sub>2</sub>. *Nat. Nanotechnol.*, **2008**, *3*, 206-209.
- S13. Lee, D.; Kwon, G. D.; Kim, J. H.; Moyon, E.; Lee, Y. H.; Baik, S.; Pribat, D. Significant Enhancement of the Electrical Transport Properties of Graphene Films by Controlling the Surface Roughness of Cu Foils Before and During Chemical Vapor Deposition. *Nanoscale*, **2014**, *6*, 12943-12951.
- S14. Chan, S.-H.; Chen, J.-W.; Chen, H.-P.; Wei, H.-S.; Li, M.-C.; Chen, S.-H.; Lee, C.-C.; Kuo, C.-C. The Deviation of Growth Model for Transparent Conductive Graphene. *Nanoscale Res. Lett.*, **2014**, *9*, 581.
- S15. Kim, H.; Bae, S.-H.; Han, T.-H.; Lim, K.-G.; Ahn, J.-H.; Lee, T.-W. Organic Solar Cells Using CVD-Grown Graphene Electrodes. *Nanotechnology*, **2014**, *25*, 014012.
- S16. Kwon, K. C.; Ham, J.; Kim, S.; Lee, J.-L.; Kim, S. Y. Eco-Friendly Graphene Synthesis on Cu Foil Electroplated by Reusing Cu Etchants. *Sci. Rep.*, **2014**, *4*, 4830.
- S17. Meyer, J.; Kidambi, P. R.; Bayer, B. C.; Weijtens, C.; Kuhn, A.; Centeno, A.; Pesquera, A.; Zurutuza, A.; Robertson, J.; Hofmann, S. Metal Oxide Induced Charge Transfer Doping and Band Alignment of Graphene Electrodes for Efficient Organic Light Emitting Diodes. *Sci. Rep.*, **2014**, *4*, 5380.
- S18. Suk, J. W.; Kitt, A.; Magnuson, C. W.; Hao, Y.; Ahmed, S.; An, J.; Swan, A. K.; Goldberg, B. B.; Ruoff, R. S. Transfer of CVD-Grown Monolayer Graphene onto Arbitrary Substrates. *ACS Nano*, **2011**, *5*, 6916-6924.
- S19. Kim, K.; Lee, H.-B.-R.; Johnson, R. W.; Tanskanen, J. T.; Liu, N.; Kim, M.-G.; Pang, C.; Ahn, C.; Bent, S. F.; Bao, Z. Selective Metal Deposition at Graphene Line Defects by

Atomic Layer Deposition. *Nat. Commun.*, **2014**, *5*, 4781.

- S20. Li, X.; Zhu, Y.; Cai, W.; Borysiak, M.; Han, B.; Chen, D.; Piner, R. D.; Colombo, L.; Ruoff, R. S. Transfer of Large-Area Graphene Films for High-Performance Transparent Conductive Electrodes. *Nano Lett.*, **2009**, *9*, 4359-4363.